Available online at website: https://journal.bcrec.id/index.php/bcrec

Bulletin of Chemical Reaction Engineering & Catalysis, 21 (1) 2026, 191-212

Original Research Article

Ceria-Promoted Titanium Dioxide (CeO_2/TiO_2) Nanocomposites for Efficient Phenol Removal under Advanced Oxidation Processes (AOPs)

Farah Guitouni[1], Ilhem Rekkab-Hammoumraoui[*,1], Sanaa El Korso[1], Mohamed Sassi[2], Chewki Ziani-Cherif[1]

[1]*Laboratory of Catalysis and Synthesis in Organic Chemistry (LCSCO) Abou Bekr Belkaid University of Tlemcen, BP 119, 13000 Tlemcen, Algeria.*
[2]*Laboratory of Materials Chemistry (LCM), University Oran1 "Ahmed Ben Bella", BP 1524, El-Menaouer, 31000 Oran, Algeria.*

Received: 9th December 2025; Revised: 6th January 2026; Accepted: 7th January 2026
Available online: 17th January 2026; Published regularly: April 2026

Abstract

In this study, a series of x %CeO_2/TiO_2 (x= 1, 2, 3, 5 and 10) catalysts were successfully synthesized with $Ce(NO_3)_3.6H_2O$ as precursor via a simple wetness impregnation method. The resulting samples were characterized by XRD, FTIR, surface area and pore volume measurements, Raman spectroscopy, SEM, and UV-Vis -DRS. These catalysts were used for the degradation of the phenol through three types of advanced oxidation processes (AOPs), namely the heterogeneous Fenton process (photocatalyst/H_2O_2), the photocatalysis process (photocatalyst/UV), and the photo-Fenton process (photocatalyst/UV/H_2O_2). The 10 % CeO_2/TiO_2 catalyst showed superior degradation efficiency of 99.05 %, when used in the heterogeneous photo-Fenton process. To determine the optimal conditions for phenol degradation, using the heterogeneous photo-Fenton process, the effects of parameters such as photocatalyst dosage, initial pH, phenol concentration, H_2O_2 volume, and temperature were investigated. The optimal conditions were as follows: 0.1 g of catalyst, 0.6 mM of hydrogen peroxide, a reaction temperature of 25 °C, an initial pH of 8, an initial phenol concentration of 30 ppm, and a reaction time of 240 minutes. The impact of radical scavengers (such as p-benzonquinone, silver nitrate, EDTA-2Na and propan-2-ol) on degradation efficiency was also studied. For all three oxidation processes, phenol photodegradation could be described by the pseudo-first-order kinetics according to the Langmuir-Hinshelwood model. Furthermore, the catalysts could be easily recovered from the reaction solution by centrifugation and reused for five cycles without significant loss of activity.

Keywords: Cerium doped titanium dioxide; Phenol; Advanced oxidation processes; Hydrogen peroxide; UV irradiation

How to Cite: Guitouni, F., Rekkab-Hammoumraoui, I., El Korso, S., Sassi, M., Ziani-Cherif, C. (2026). Ceria-Promoted Titanium Dioxide (CeO_2/TiO_2) Nanocomposites for Efficient Phenol Removal under Advanced Oxidation Processes (AOPs). *Bulletin of Chemical Reaction Engineering & Catalysis*, 21 (1), 191-212. (DOI: 10.9767/bcrec.20545)

Permalink/DOI: https://doi.org/10.9767/bcrec.20545

1. Introduction

Phenols, recognized as some of the most toxic organic pollutants, are discharged into wastewater by numerous industries, including agriculture, petrochemicals, textiles, paints, plastics, and pesticides [1]. These harmful, persistent compounds cause undesirable tastes and odors in both ground and surface waters [2-4]. Their toxicity and resistance to biodegradation present a significant threat to environmental integrity and human health, potentially leading to major economic and financial consequences [5,6]. With a global annual production of about 7 million tons due to widespread industrial applications, phenol is found in high concentrations in the effluents of industries such as coke ovens, phenolic resins, and coal conversion [7]. Even at low levels, phenols can be harmful to a variety of organisms and can cause severe health issues [8]. Consequently, the World Health Organization

* Corresponding Author.
Email: rekkabilhem2017@gmail.com ; ilhem.hammoumiraoui@univ-tlemcen.dz (I. Rekkab-Hammoumraoui)

(WHO) has established strict limits for phenol in drinking water, with a maximum permissible concentration of 1–2 μg/L [9].

Several treatment methods have been explored for the removal and degradation of phenolic compounds in wastewater, such as chemical precipitation [10], separation [11], adsorption [10], coagulation [12], and biodegradation [13]. However, these methods often only lead to partial degradation, shifting contaminants between phases and generating secondary pollutants that require further treatment [14,15]. Recently, advanced oxidation processes (AOPs), which use semiconducting materials as photocatalysts exposed to light, have gained attention for their ability to degrade persistent organic pollutants. These photocatalysts, such as TiO_2, CdS, ZnO, SnO_2, and CeO_2, possess a unique electronic band structure with a valence band and conduction band separated by an energy bandgap (Eg). When photons with energy greater than or equal to the bandgap are absorbed, electron–hole (e^-/h^+) pairs are generated within the semiconductor particles. These photogenerated carriers migrate, causing charge separation and producing strong oxidizing agents (e.g., $\bullet O_2^-$, e^-, h^+, and $\cdot OH$), which initiate the degradation of organic pollutants, ultimately mineralizing them into CO_2, water, and mineral acids [16,17].

Among these semiconductors, TiO_2 is particularly efficient, nontoxic, cost-effective, and stable over a wide pH range [18-21]. Despite its potential, the practical catalytic performance of TiO_2 is severely restricted by its large band gap (3.2 eV for anatase and 3.0 eV for rutile) [22]. Additionally, TiO_2's photocatalytic efficiency is often limited by a high rate of electron-hole recombination [23,24]. Ceria (CeO_2), a rare earth element, has attracted significant interest for environmental remediation due to its high oxygen storage capacity (OSC) and thermal stability [25-27]. Its ability to switch between two oxidation states (Ce^{3+}/Ce^{4+}) and form oxygen vacancies enhances its redox behavior [25,28-32]. Metal doping, such as doping TiO_2 with ceria, reduces the bandgap energy [33], inhibits electron-hole recombination, and broadens the light absorption range, thereby improving photocatalytic efficiency [34-36]. Although CeO_2/TiO_2 catalysts have been widely investigated, most studies have focused on single-process applications. As a result, their comparative performance across different advanced oxidation processes (AOPs) remains insufficiently explored. In particular, there is a lack of systematic investigations examining how these materials behave when transitioning between photocatalytic, Fenton, and photo-Fenton systems under identical operating conditions. Against this backdrop, our results reveal the distinctive dual role of CeO_2. On the one hand, it effectively limits electron–hole recombination, and on the other, it actively facilitates the activation of H_2O_2.

The originality of this work lies in overcoming these limitations through a comprehensive comparative evaluation of three heterogeneous AOPs. Rather than treating the material as a simple doped semiconductor, this study highlights the dual nature of CeO_2, showing that it functions both as a promoter of charge separation and as a highly efficient catalytic site for H_2O_2 activation. By integrating these mechanistic insights with detailed kinetic modeling based on the Langmuir–Hinshelwood approach, this work offers a clearer understanding of the synergistic pathways governing the mineralization of phenol.

In this study, CeO_2/TiO_2 photocatalysts with varying CeO_2 loadings (1–10 %) were synthesized using liquid impregnation and characterized using techniques like Fourier-transform infrared spectroscopy (FTIR), powder X-ray diffraction (XRD), BET analysis, UV-vis diffuse reflectance spectroscopy (DRS), Raman spectroscopy, and scanning electron microscopy (SEM). The phenol degradation performance of the photocatalysts was evaluated using three heterogeneous advanced oxidation processes: the heterogeneous Fenton (photocatalyst/H_2O_2), photocatalysis (photocatalyst/UV), and photo-Fenton (H_2O_2/photocatalyst/UV) processes. The study also explored the synergistic effects of phenol degradation in photo-Fenton reactions, varying parameters such as photocatalyst dosage, initial pH, phenol concentration, H_2O_2 volume, and temperature. UV-Vis spectroscopy was used to analyze the photocatalytic degradation results, determine optimal conditions, and conduct kinetic studies using the Langmuir-Hinshelwood (L-H) kinetic model.

2. Materials and Methods

2.1 Materials

All chemicals used in the experiments were of analytical grade, purchased from Sigma Aldrich and used as received without further purification. (TiO_2, anatase, 97 %, M = 79.87 $g.mol^{-1}$), ($Ce(NO_3)_3.6H_2O$, ≥ 99 %, M = 434.22 $g.mol^{-1}$), (H_2O_2, 30 %, M = 34 $g.mol^{-1}$), (NaOH, 98 %, M = 40 $g.mol^{-1}$), (HCl, 37 %, d = 0.789, M = 36.46 $g.mol^{-1}$), (C_6H_6O, M = 94.11 $g.mol^{-1}$).

2.2. Catalyst Preparation

The CeO_2/TiO_2 catalyst was synthesized via the incipient wetness impregnation method. First, TiO_2 (Degussa P25 calcined at 400 °C for 4 h) was placed and stirred in water to form a homogenous suspension. A proper amount of $Ce(NO_3)_3.6H_2O$ was dissolved in 10 mL of distilled water to form a transparent solution, and then added to TiO_2

suspension, with stirring for 24 h at room temperature. The mixture undergoes two drying processes: first, for four hours in a sand bath at 80 °C, then overnight at 100 °C in the oven. The obtained solids were then calcined at 400 °C in air for 4 h with ramp rate of 5 °C /min. The amount of CeO_2 was varied from 1 % to 10 % by the changing the amount of cerium nitrate hexahydrate during the synthesis.

2.3. Catalysts Characterizations

X-ray powder diffraction (XRD) patterns of the samples were recorded on a Rigaku D-MiniFlex Nifil-tered 600 powder X-ray diffractometer with Cu-Kα (λ = 1.541874 Å), in the 2θ range of 20 ° - 80 °, with a step size of 0.03 ° and a scan speed of 2 °/min. The N_2 physisorption measurement was carried out in a Micromeritics 3flex at 77.35 K. Before the analysis, the catalyst samples were degassed at 200 °C for 2 h in vacuum. The specific surface area was calculated by Brunauer-Emmett-Teller (BET) equation, while the pore size and pore volume distributions were determined from desorption isotherms using Barrett-Joyner-Halenda (BJH) method. Fourier-transform infrared (FTIR) spectra were conducted using an Agilent Technologies Cary 600 FTIR spectrometer in the range of 400–4000 cm^{-1} using KBr pallet method. The UV-vis diffuse reflectance spectra (DRS) of the samples in the 200 - 800 nm range were recorded on an Agilent Carry 7000, Universal Measurement Spectrophotometer equipped with an integrating sphere attachment, using $BaSO_4$ as the reflectance standard. A Hitachi TM1000 Scanning Electron Microscope (SEM) was used to characterize the morphological features of the synthesized catalysts. The Energy Dispersive X-ray (EDX) spectrum of the samples was also recorded in the same instrument and the chemical composition was studied. The measurements of Raman spectroscopy were performed at room temperature using HORIBA Scientific (LabRAM HR Evolution) Raman spectrometer, using a λ = 633 nm laser line as the excitation source with spectral resolution of 2 cm^{-1} in a scanning range of 20–1000 cm^{-1}. Analytik Jena SPECORD 210 PLUS spectrophotometer was used to analyze phenol solution samples obtained from Heterogeneous Fenton, photocatalysis, and photo-Fenton experiments. Spectral scanning was acquired between 200 and 800 nm range at a speed of 20 nm/s. The maximum absorbance of phenol was found at 272 nm.

2.4. Degradation Processes

2.4.1 Heterogeneous Fenton

Phenol degradation experiments were performed in a 250 mL Erlenmeyer flask. 130 mL of phenol solution 30 ppm containing 0.1 g of catalyst was stirred at ambient temperature for 60 minutes to achieve adsorption-desorption equilibrium. Subsequently, 0.6 mM of 30 % H_2O_2 was then added to initiate the reaction. Samples (2 mL) were collected every 10 minutes, centrifuged, and analyzed for phenol concentration by measuring absorbance at 272 nm using a UV-Vis spectrophotometer Analytik Jena SPECORD 210 PLUS. All experiments were conducted in duplicate or triplicate for reproducibility.

2.4.2 Photocatalysis

Photocatalytic degradation experiments were performed in a three-neck flask. The 0.1 g of catalyst was placed in a volume of 130 mL of phenol solution and stirred for 60 minutes in the dark until the adsorption–desorption equilibrium was obtained. UV irradiation was then carried out using a 10 W pen lamp (λ = 254 nm, 6.5 mm diameter, 53.8 mm length) enclosed in a quartz jacket immersed in the solution. A UV–visible spectrophotometer model Analytik Jena SPECORD 210 PLUS was used to measure the sample absorbance during the manipulation.

2.4.3 Heterogeneous Photo-Fenton

The experiments carried out in this process are similar to those of photocatalysis. However, after 60 minutes of stirring in the dark, in addition to the illumination by the UV lamp, an amount of H_2O_2 was injected into the reaction system, marking the start of the reaction (t_0). The percentage of phenol degradation (Efficiency) was calculated using Equation (1):

$$Efficiency\ (\%) = \frac{A_0 - A_t}{A_0} \times 100\% = \frac{C_0 - C_t}{C_0} \times 100\% \quad (1)$$

where, A_0 and A_t represent the absorbance values of the solution before degradation (after 60 min of adsorption) and at specific time intervals, respectively. Similarly, C_0 corresponds to the initial concentration of phenol, while C_t is the concentration at a specific time. The adsorption percentage (%) was determined using the same equation.

3. Results and Discussion

3.1. Catalyst Characterizations

3.1.1. X-Ray Diffraction

The XRD analysis was conducted to determine the crystalline and phase of CeO_2/TiO_2 with different CeO_2 loadings. Figure 1a shows the XRD graphics of the samples. The observed 2θ values at 25.24°, 37.78°, 48.02°, 53.9°, 55.1°, 62.86°, 68.93°, 70.24°, and 75.11° can be matched to the (101), (004), (200), (105), (211), (204), (116),

(200), and (215) planes, respectively. All these peaks belong to anatase phase of TiO_2 which crystallized in the tetragonal structure and matches well with the standard JCPDS card no. 84-1285. It is noteworthy that the XRD spectra of sample containing 1 wt% ceria did not exhibit any discernible peaks attributable to cerium oxide. It could typically be attributed to three factors: low CeO_2 content with high dispersion, the presence of very small CeO_2 crystallites (< 5 nm), or the existence of amorphous CeO_2 [37,38]. A small cerium oxide peak at $2\theta = 28°$ was evident in the spectra for 3 and 5 wt% loadings. Furthermore, a second peak at $2\theta = 33.08°$ was distinctly observed for 10 wt% loading. These peaks can be indexed to the (111) and (200) planes of cubic fluorite CeO_2, respectively, based on JCPDS PDF no. 34-0394 [39].

Spectral analysis reveals a gradual attenuation of the anatase (101) peak intensity with increasing Ce concentration in the samples. Crystal size, determined using Scherrer's formula on the anatase (101) diffraction plane demonstrate a clear inverse relationship between Ce concentration and crystal size. This observation can be explained by the formation of Ce-O-Ti bonds on the catalyst surface, which inhibit crystal grain growth Table 1 [40-42]. The XRD pattern shows that the peaks of doped samples are slightly shifted towards the higher diffraction angle side. This shift, particularly evident for the (101) plane, suggests the incorporation of Ce into the TiO_2 lattice. However, the size mismatch between Ti^{4+} (0.065 nm) and Ce^{3+}/Ce^{4+} (0.103 nm/ 0.101 nm) cations restrict Ce substitution at Ti sites [40,43]. Hence, relatively large Ce cations stay on the particle surfaces, and at grain boundaries and grain junctions. This may inhibit the crystallite growth of titania through the formation of Ce–O–Ti bonds, which increase the diffusion barrier at the titania grain junctions [44]. It can be seen that the intensity of the XRD peaks Figure 1a decreases by increasing the Ce content, which might be due to a decrease in the average particle size caused by the doping. Cano-Franco *et al.* [36] proposed that Ce can substitute for oxygen (0.132 nm) in the crystal TiO_2 lattice, resulting in the formation of oxygen vacancies and lattice distortion.

3.1.2 BET analysis

The textural properties of the resulting materials, including surface area and pore size distribution, were characterized by nitrogen adsorption-desorption isotherm analysis and the corresponding data are presented in Figure 2a. The curves of the N_2 adsorption-desorption isotherms for all samples were similar, in which x %CeO_2/TiO_2 exhibited a type IIb isotherm according to IUPAC classification [45] reflecting the presence of low porous or macroporous samples (pore sizes exceeding 50 nm), with a type

Table 1. Textural properties of various catalysts.

Catalyst	BET surface area ($m^2.g^{-1}$)	Pore volume ($cm^3.g^{-1}$)	Average pore diameter (nm)	Particles Size (nm)
TiO_2	10	0.15	67	67
1% CeO_2/TiO_2	10	0.21	58	57
2% CeO_2/TiO_2	11	0.16	61	55
3% CeO_2/TiO_2	12	0.17	60	48
5% CeO_2/TiO_2	13	0.18	54	47
10% CeO_2/TiO_2	19	0.18	39	36

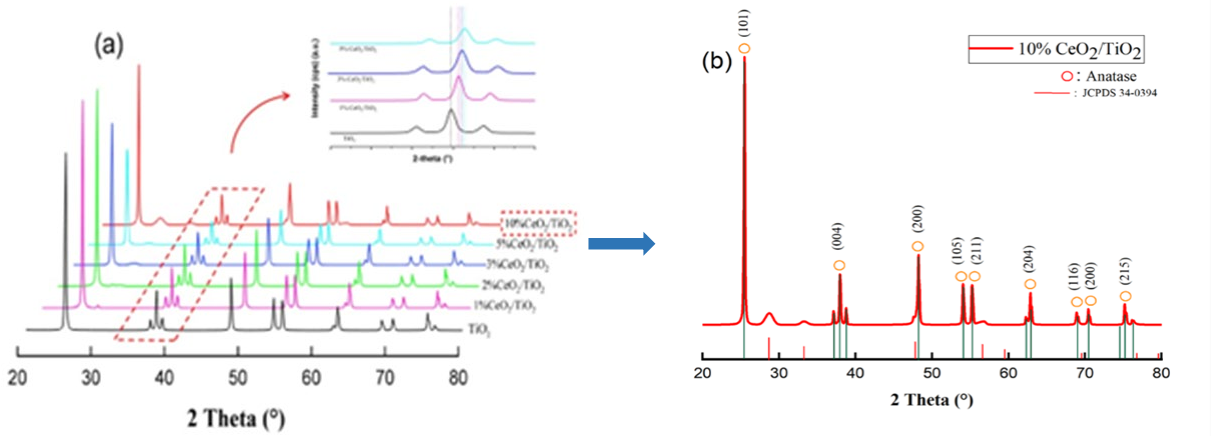

Figure 1. XRD patterns of CeO_2/TiO_2 materials with diverse CeO_2 dosages.

H3 hysteresis loop. The pore-size distribution Figure 2b revealed the presence of both mesopores and macropores (the pore size value is at upper mesopore and lower macropore margin). Table 1 summarizes the surface area, pore volume and average pore diameter of the samples. A slight increase in surface area was observed with increasing Ce content (from 1 % to 10 %), likely attributed to CeO_2 inhibiting the agglomeration of TiO_2 crystallites [46]. This is consistent with XRD results in Figure 1a, which suggest a decrease in crystallinity due to the incorporation of CeO_2, which hinders crystal growth and sintering processes [47]. While the pore volume increased mildly, the overall mesopore/macropore structure was well-maintained in the composites. This favorable pore structure facilitated the adsorption and reaction of organic pollutants, as well as enhanced electron transfer within the materials [43]. The presence of a relatively large particle surface area increases the number of active sites available for reactant adsorption, thereby making the photocatalytic process more effective [48].

3.1.3 FTIR analysis

Figure 3a presents the IR spectra of TiO_2 and x %CeO_2/TiO_2 materials. The high-frequency region (3600-3200 cm^{-1}) is typically associated with OH vibrations, while lower frequencies correspond to Ti–O and Ce–O bond vibrations [49-51]. According to McDevitt *et al.* [52], the vibrations observed between 800 and 400 cm^{-1} are attributed to the stretching vibrations ν (Ti–O) of the −[Ti–O–Ti–O–Ti–O]− chain. Furthermore, Larbot *et al.* [53] and Chhor *et al.* [54] subdivided this frequency range into two regions: ν = 653-550 cm^{-1}, assigned to the stretching vibrations of isolated Ti–O bonds. ν = 495-436 cm^{-1}, attributed to the stretching vibrations of Ti–O bonds within the −[Ti–O–Ti–O–Ti–O]− chain.

The IR spectrum exhibits a broad band centered at 3450 cm^{-1} attributed to both water bending vibrations and asymmetric Ti-OH stretching [55-57]. A distinct band at 2363 cm^{-1} corresponds to the asymmetric stretching vibrations of atmospheric CO_2 [58]. In the 1500-400 cm^{-1} region Figure 3b, two absorption regions

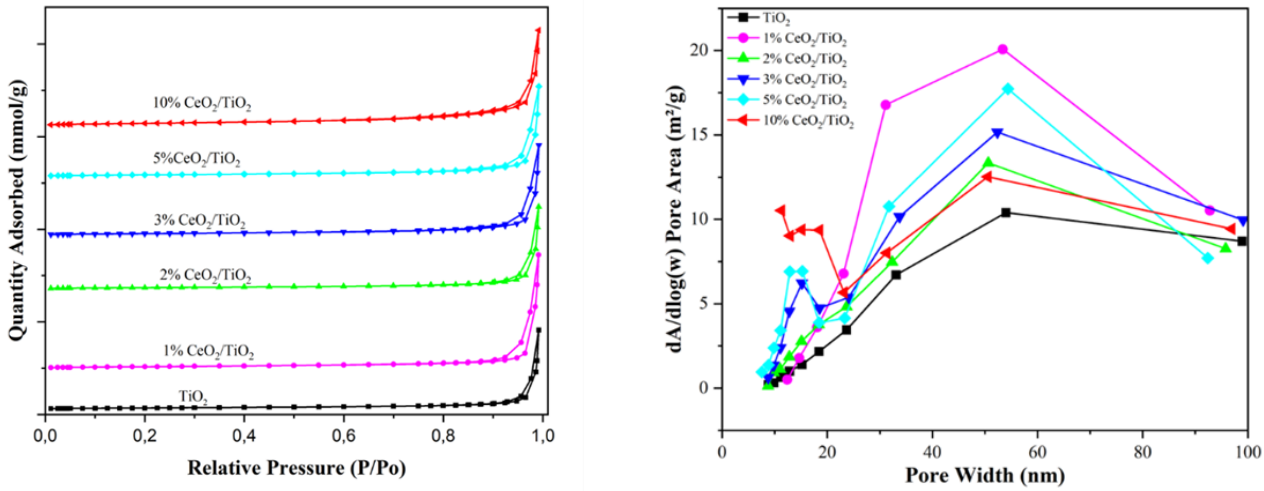

Figure 2. N_2 adsorption–desorption isotherms (a) and BJH-pore size distribution of the supported samples (b).

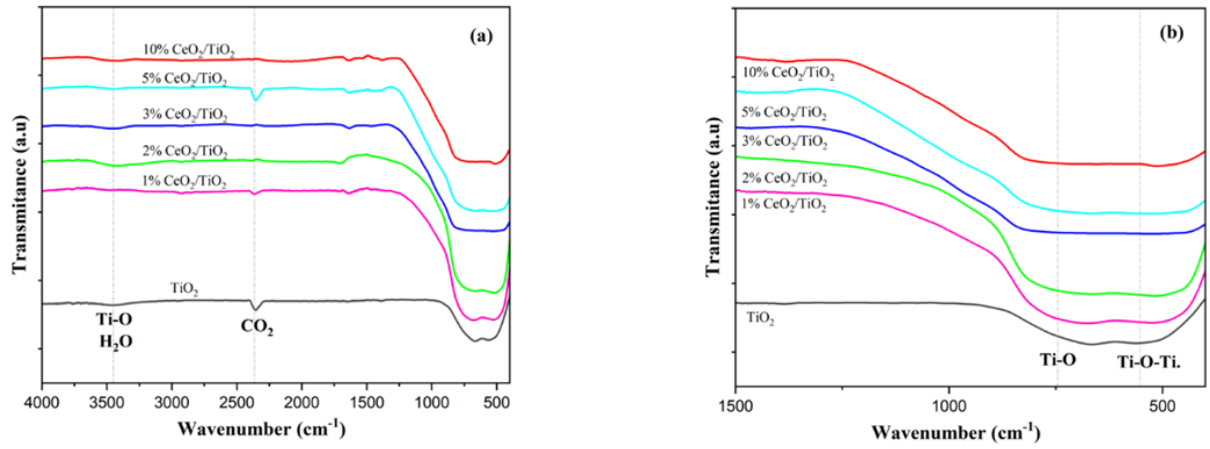

Figure 3. FTIR spectra of various samples.

are observed: 750-650 cm^{-1} assigned to Ti-O stretching in simpler molecular arrangements, and 610-450 cm^{-1} characteristic of Ti-O-Ti bridge stretching. The Ce-O stretching vibration, expected in this region, is likely obscured by the intense Ti-O-Ti band [59]. In the infrared absorption spectrum of 10%CeO_2/TiO_2, the characteristic TiO_2 peak at 540 cm^{-1} shifts to approximately 565 cm^{-1}. This shift suggests that the incorporation of Ce into the TiO_2 lattice, leading to the formation of Ti-O-Ce bonds, alters the stretching vibrations of the original Ti-O-Ti bonds.

3.1.4 Raman spectral analysis

Raman spectra of TiO_2, CeO_2 and various CeO_2/TiO_2 mixed oxides are displayed in Figure 4a. The Raman bands pertaining to the anatase phase are observed at 140,87 (Eg), 192,50 (Eg), 392,49 (B1g), 512,50 (A1g + B1g) and 635,00 (Eg) cm^{-1}. Eg modes originate from symmetric stretching vibrations of oxygen atoms within the O-Ti-O bond, whereas B1g and A1g modes arise from symmetric and anti -symmetric bending vibrations of O–Ti–O bond [60,61]. The Raman spectrum of CeO_2, a fluorite-structured material, exhibits a prominent F2g mode at 462 cm^{-1} [62,63]. This mode emanates from symmetric vibrations of oxygen atoms within the Ce-O-Ce framework. Additionally, weaker features are observed at 260 cm^{-1} and 600 cm^{-1}, corresponding to the normally Raman-inactive (IR-active) transverse and longitudinal optical phonon modes at the Brillouin zone center (Figure 4b). As the Ce weight percentage increases, a gradual decrease in the intensity of all Raman peaks is observed, and the prominent Eg peak exhibits a slight blue-shift. The observed Eg peak positions are: 142.43 cm^{-1} (1%CeO_2/TiO_2), 142.11 cm^{-1} (2%CeO_2/TiO_2), 143.44 cm^{-1} (3%CeO_2/TiO_2), 146.13 cm^{-1} (5%CeO_2/TiO_2), and 147.19 cm^{-1} (10%CeO_2/TiO_2), respectively (Figure 4c). Consistent with XRD results, the Raman spectra of CeO_2/TiO_2 mixed oxides with low Ce/TiO_2 weight ratios do not display the characteristic Raman band of cubic CeO_2. This band becomes apparent in the mixed oxides with CeO_2/TiO_2 weight ratios of 5 and 10 % [64]. The ionic radius mismatch between Ce and Ti leads to lattice distortion in TiO_2 when Ce enters interstitial sites. Ce^{3+} incorporation into the TiO_2 matrix generates oxygen vacancies, potentially facilitated by electron transfer between Ce^{3+} and Ce^{4+}. Higher Ce^{3+} concentrations likely result in increased oxygen vacancy formation. These oxygen vacancies can induce lattice distortions and consequently shift the Raman peaks to higher wavenumbers [65,66]. Additionally, the presence of oxygen vacancies (lattice defects) caused by the displacement of oxide ions from their normal lattice sites contributes to the broadening and shifting of Raman active modes. Moreover, size-induced radial pressure in nanocomposites leads to volume contraction and increased force constants, resulting in a blue-shift of the Raman peaks [65,67]. The results from Raman spectra are following the results of XRD.

3.1.5 UV–vis-diffuse reflectance spectroscopy (UV–vis-DRS)

The diffuse reflectance spectra of bare TiO_2 and x %CeO_2/TiO_2, recorded at room temperature,

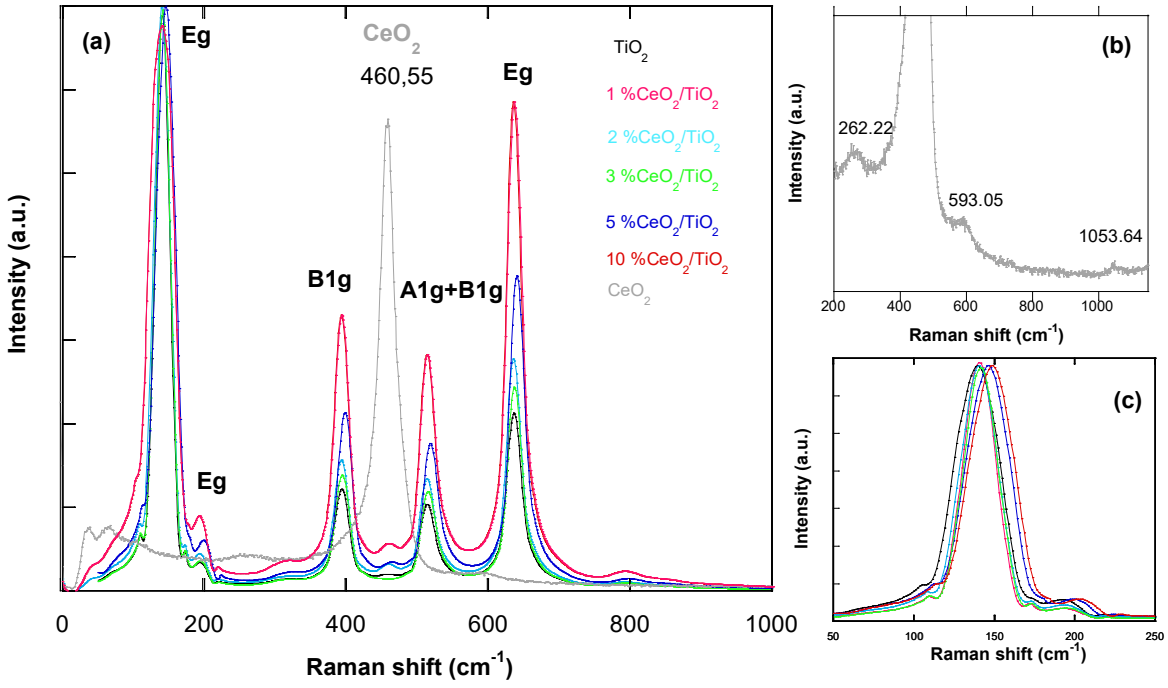

Figure 4. Raman spectra of 1-10 %CeO_2/TiO_2 mixed oxides.

are shown in Figure 5a. TiO_2 mainly absorbs ultraviolet (UV) light, and its maximum wavelength is 380 nm which corresponds to $O^{2-} \rightarrow Ti^{4+}$ charge transfer and related to electron excitation from valence band to the conduction band in TiO_2 [68]. However, the absorption edge was found to be shifted to higher wavelengths (red shift) after CeO_2 incorporation, and it continuously showed a small shift with the incremental loading of CeO_2 in the samples. The absorption edges of Ce-doped samples with a concentration of 1 %, 2 %, 3 %, 5 % and 10 % were observed at 387 nm, 390 nm, 386 nm, 392 nm and 397 nm, respectively. The red shift is likely attributed to the formation of heterojunction between TiO_2 and CeO_2 via their interaction or close contact in the composite [69]. Noteworthy, the red shift may be caused by the formation a new electronic state, which reduces the distance of charge transfer between 4f electrons of Ce ions and the conduction or valence band in the TiO_2 bandgap, enhancing the photocatalytic activity [70]. The energy gaps of the as-prepared materials were determined using the Tauc plot method and are presented in Figure 5b. The band gap energy (Eg) was calculated using the following equation [71]:

$$(\alpha h\nu)^n = A\,(h\nu - Eg) \qquad (2)$$

where, α is the absorption coefficient, h is Planck's constant, ν is the optical frequency, and A is a constant. The exponent 'n' depends on the type of semiconductor transition: 1/2 for indirect transitions and 2 for direct transitions. Since TiO_2 is an indirect-band gap semiconductor, n = 1/2 [72]. The calculated band gaps for pure CeO_2, pure TiO_2 and (1-10)% CeO_2/TiO_2 were determined to be 2,81 eV, 3.26 eV, 3.20 eV, 3.18 eV, 3.21 eV, 3.16 eV and 3.12 eV, respectively. The observed band gap for the TiO_2 is in excellent agreement with the literature values reported for the anatase [22]. The results show that the lowest band gap energy (Eg) of the semiconductors corresponds to that in the solids with the highest cerium content. At such concentrations, the maximum substitution of Ti^{4+} by Ce^{4+} cations could be reached. These results do not imply that all the cerium added to the titania substituted the Ti^{4+} cations in the titania framework. It illustrates that the maximum substitution, probably just a few titanium cations, is reached with such cerium contents. In fact, we cannot expect a high substitution of Ti^{4+} by Ce^{4+} cations, since the ionic radius of Ti^{4+} is lower (0.065 nm) than that of Ce^{4+} (0.101 nm) [43]. These results indicate that doping Ce in TiO_2 significantly reduces the band gap energy and effectively inhibits the recombination of photogenerated electron holes [44].

3.1.6 SEM analysis

The Scanning Electron Microscopy (SEM) images of TiO_2 and CeO_2/TiO_2 with varying CeO_2 loadings are presented in Figure 6. The SEM image in Figure 6a reveals that the majority of TiO_2 particles exhibit a combination of homogeneous and irregular crystalline structures at the nanoscale. Furthermore, all observed particles tend to aggregate, forming clusters that adhere to each other with diverse shapes and sizes. CeO_2 incorporation (1-10 wt.%) into TiO_2, as shown in Figure 6 (b)–(f), led to the formation of larger agglomerates. Increasing CeO_2 loading further enhanced agglomeration while simultaneously increasing the porosity of the composites, characterized by a network of interconnected voids [73]. This morphology is expected to enhance the catalytic properties of the material. [24]. The EDX analysis, as shown in Figure 6 (a)-(f), reveals the presence of peaks corresponding exclusively to Ce and Ti [43,44]. The absence of any other elemental peaks strongly

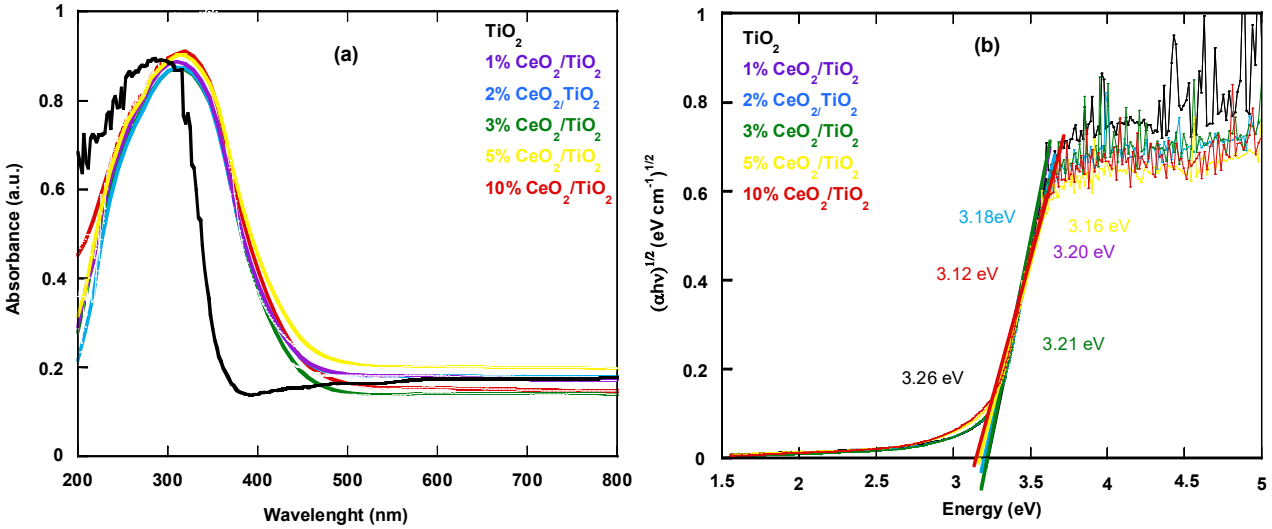

Figure 5. DR UV – vis spectra (a) and Tauc plots (b) of the as-prepared samples.

suggests that the synthesized sample is highly pure and free from any significant impurities [39]. EDX-estimated elemental analysis in mass ratio (Table 2) closely matches the theoretical ratio. This deviation is completely acceptable.

3.2. Catalytic Tests

The catalytic performances of the catalysts were investigated by assessing their ability to degrade phenol through Heterogeneous Fenton, photocatalytic, and photo-Fenton reactions in aqueous media.

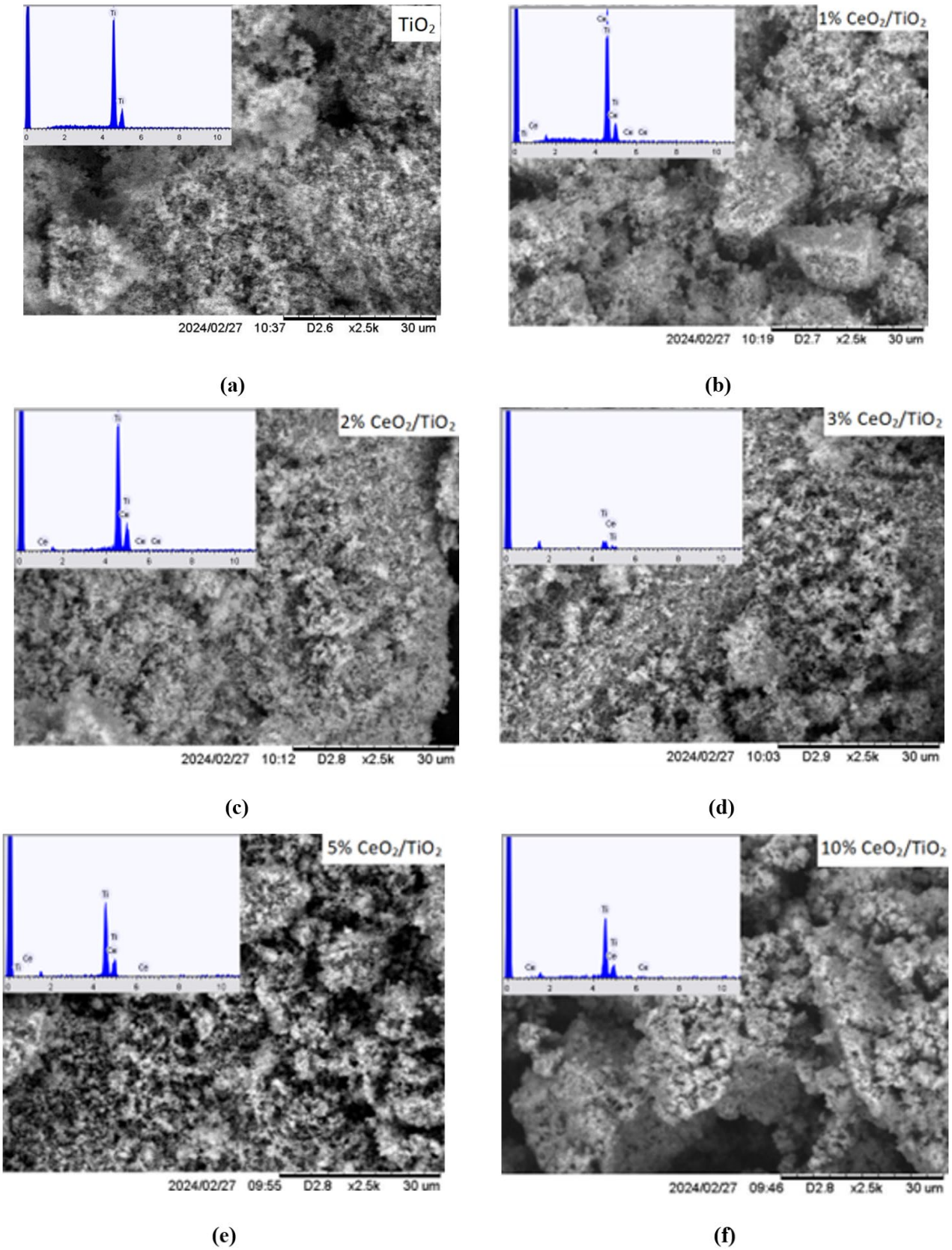

Figure 6. SEM graphics of samples.

3.2.1 Adsorption and blank tests

Before photocatalytic experiments, the adsorption capacity of the catalysts for phenol was determined under conditions identical to those employed in subsequent photocatalytic studies. Figure 7a illustrates the phenol adsorption on samples after 2 hours in the dark. Nearly 14.1 %, 14.7 %, 16.6 %, 17.9 %, 18.5 % and 22.5 % phenol adsorption was measured for TiO_2, 1 %, 2 %, 3 %, 5 % and 10 %CeO_2/TiO_2 catalysts respectively. Equilibrium was generally reached within 60 minutes, with adsorption being rapid initially and then slowing down. The 10 %CeO_2/TiO_2 material, exhibiting the largest specific surface area (19 m^2/g), demonstrated the highest adsorption capacity. [37,74]. Notably, the TiO_2 support and 1 %CeO_2/TiO_2 material displayed nearly identical adsorption capacities, likely due to the low ceria content in the latter, which had a minimal impact on its specific surface area. Consequently, a 60-minute equilibration period was implemented prior to each catalytic reaction.

The direct photolysis in heterogeneous Fenton and photocatalysis reactions resulted in the lowest phenol degradation in aqueous solution, with only 4.5 % and 21.64 % degradation respectively. In contrast, under photo-Fenton conditions, photolysis achieved a degradation rate of 77.88 % (Figure 7b).

Table 2. Phenol adsorption (without UV irradiation) (a), and Photolysis (b). (25 °C, 0.1 g of catalyst, and 30 ppm phenol pH of 7).

Sample	Composition weight (%)	
	Ce	Ti
TiO_2	0	100
1%CeO_2/TiO_2	0.96	99.04
2%CeO_2/TiO_2	1.75	98.25
3%CeO_2/TiO_2	3.37	96.63
5%CeO_2/TiO_2	4.71	95.29
10%CeO_2/TiO_2	9.99	90.01

3.2.2 Phenol catalytic degradation

According to Figure 8a, the heterogeneous Fenton reaction (H_2O_2/catalyst) appears to be ineffective with all of the prepared catalysts. Pure titanium dioxide (TiO_2) exhibited the highest performance for phenol degradation, achieving approximately 32.42 % degradation efficiency. This performance can be attributed to the presence of numerous active sites on the TiO_2 surface, which facilitate the formation of hydroxyl radicals (•OH), contributing to substrate degradation [75,76]. However, the oxidation ability of H_2O_2 is inherently limited [77,78]. Conversely, increasing the ceria (CeO_2) content on the TiO_2 support led to a decrease in degradation efficiency. This suggests that the ceria particles may be blocking the active sites on the TiO_2, thus hindering the generation of •OH radicals.

Figure 8b depicts the photocatalytic (catalyst/UV) degradation of phenol using different loadings of the x%CeO_2/TiO_2 catalysts. A notable increase in degradation efficiency was observed, ranging from 89.54 % with 1% CeO_2/TiO_2 to 99.77 % with 10% CeO_2/TiO_2. It is interesting to note that the 5% CeO_2/TiO_2 sample, tested several times, showed a slower initial degradation rate during the first hour of the process. This behavior suggests a temporary obstruction effect of the surface, which is highly dispersed by cerium sites, thus momentarily preventing the initial adsorption of phenol molecules or the penetration of UV rays to the active sites of catalyst during the first 60 minutes of the reaction. However, as the reaction progresses, the Ce^{3+}/Ce^{4+} redox cycles and high oxygen storage capacity effectively stabilize the generation of radicals. This allows the 5% sample

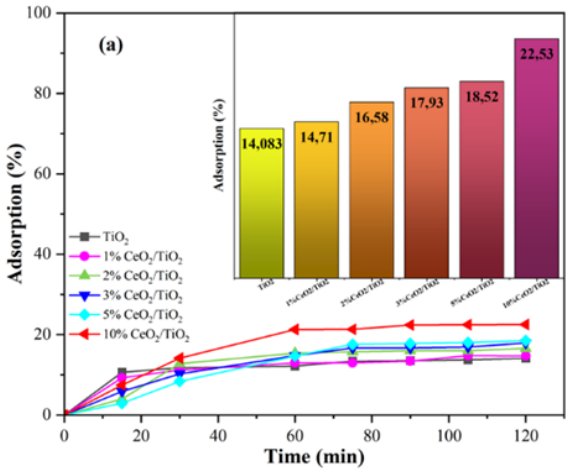

Phenol adsorption (without UV irradiation)

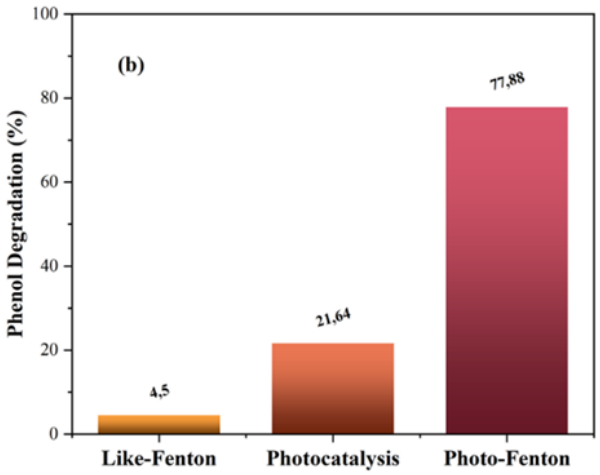

Photolysis

Figure 7. Phenol adsorption (without UV irradiation) (a), and Photolysis (b). (25 °C, 0.1 g of catalyst, and 30 ppm phenol pH of 7).

to achieve a degradation efficiency comparable to that of the 10% sample after 150 minutes. This highlights the robust synergistic effect between CeO_2 and TiO_2. The observed increase in catalytic activity with higher CeO_2 content can be attributed to the corresponding rise in specific surface area, which promotes a larger reaction interface and facilitates more rapid intraparticle molecular transfer [79,80]. The addition of CeO_2 is hypothesized to increase oxygen vacancies, which can readily capture electrons and generate surface oxygen radicals with strong reduction capabilities [81]. Ultimately, Ce^{4+} ions can capture electrons and convert them into Ce^{3+} ions [82], which possess one electron in the 4f orbital. This electron is then transferred to adsorbed oxygen, resulting in the formation of superoxide radicals that interact with and degrade phenol [83]. Additionally, the electrons trapped in Ce^{4+} sites are subsequently transferred to the adsorbed O_2 through an oxidation process, helping to prevent the recombination of photogenerated electrons and holes. A similar high degradation efficiency (99.05 %) was observed with the Photo-Fenton reaction (catalyst/H_2O_2/UV) Figure 8c. The integration of Fenton reaction and photocatalytic processes offers a distinct advantage in terms of reactive oxygen species generation. The combined

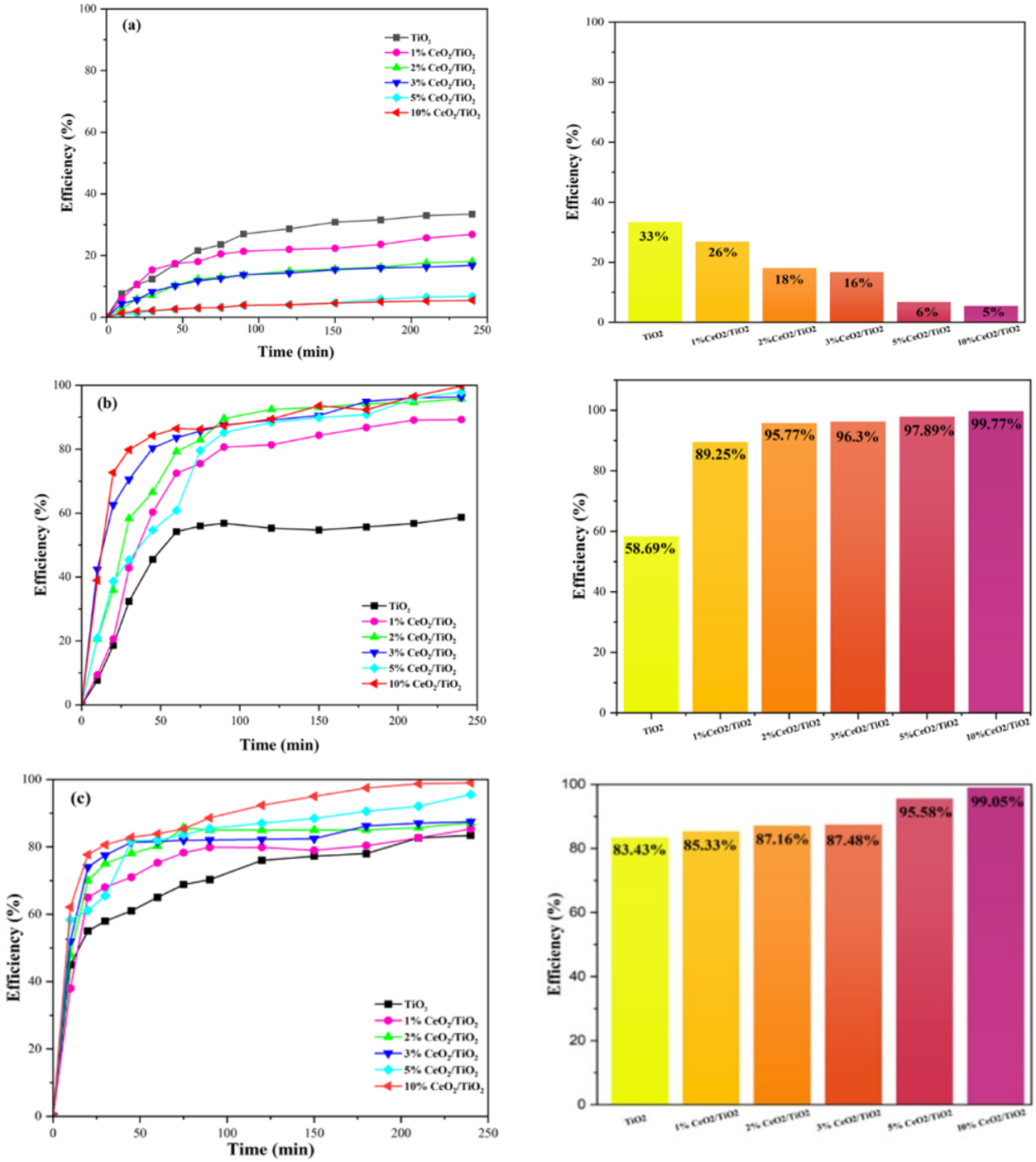

Figure 8. Kinetics of phenol degradation on the different catalysts synthesized of process (a) Like-Fenton, (b) Photocatalysis and (c) Photo-Fenton. 25 °C, 0.1 g of catalyst, 30 ppm phenol, pH 7 and H_2O_2 0.6 mM).

approach yields a significantly higher concentration of reactive oxygen species, such as singlet oxygen O_2, superoxide anions $\cdot O_2^-$, and hydroxyl radicals $\cdot OH/\cdot OOH$, compared to the application of either Fenton reactions or photocatalysis in isolation [84]. These highly reactive species are capable of disrupting the chemical bonds within organic compounds, leading to their eventual mineralization into water and carbon dioxide or substantial fragmentation into smaller, less harmful units.

First-order kinetics were used to determine reaction rates [85]. The apparent rate constants (k_{app}) and R^2 values (Figure 9) were obtained from the linear plots of $\ln(C_0/C_t)$. Table 3 summarizes the k_{app} values and calculated half-lives ($t_{1/2}$) for all AOPs. Table 3 shows a strong correlation ($R^2 \approx 0.99$), confirming that the phenol degradation follows first-order kinetics. The Fenton reaction with TiO_2 resulted in the lowest degradation rate (33.42 %), with an apparent rate constant of 0.001874 min^{-1} and a half-life of 46.47 min. Photocatalysis using 10% CeO_2/TiO_2 significantly improved the reaction rate constant by more than eight times (0.00502 min^{-1}), although the half-life increased to 137.45 min. The most effective degradation (99.05 %) was achieved with the photo-Fenton reaction using 10%CeO_2/TiO_2, which yielded the highest rate constant (0.02131 min^{-1}) and the shortest half-life (32.38 min).

3.2.3 Mechanism of photocatalytic reactions over CeO_2/TiO_2

The conduction band (CB) and valence band (VB) edge positions of CeO_2 and TiO_2 can be calculated using the Mulliken electronegativity Equations (3 and 4) [39].

$$E_{CB} = X - E_e - 0.5Eg \quad (3)$$
$$E_{VB} = X - E_e + 0.5Eg \quad (4)$$

E_{CB} represents the conduction band edge energy, E_{VB} the valence band edge energy, X the electronegativity (5.56 eV for CeO_2 and 5.81 eV for TiO_2 [34], Ee the free energy of electrons relative to the normal hydrogen electrode (NHE) (4.5 eV) [34], and Eg the semiconductor's band gap. Based on calculations from Equations. (3) and (4), TiO_2 exhibited E_{CB} and E_{VB} values of -0.32 eV and 2.94 eV, while CeO_2 showed values of -0.35 eV and 2.46 eV. The conduction and valence band edges of CeO_2 are both lower in energy than those of TiO_2. A possible mechanism for the phenol degradation, based on the band structures of CeO_2 and TiO_2, is proposed in Figure 10.

During illumination, CeO_2, an n-type semiconductor with a band gap of approximately 3.2 eV [86,87], absorbs light. This excitation promotes electrons from the interband 4f level to the conduction band, effectively reducing electron-hole recombination [88]. Due to the higher

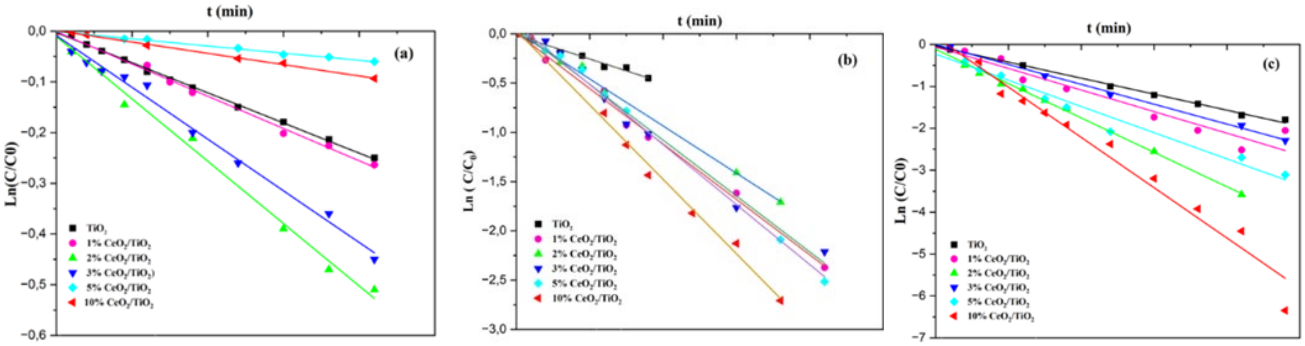

Figure 9. Temporal evolution of $\ln(C/C_0)$ for the different catalysts for all the AOPs. Like-Fenton (a), Photocatalysis (b) and Photo-Fenton (c)

Table 3. Fitting kinetics parameters of phenol degradation using 10 %CeO_2/TiO_2 according to pseudo first-order.

Catalyst	Fenton			Photocatalysis			PhotoFenton		
	k_{app} (min^{-1})	$t_{1/2}$ (min)	R^2	k_{app} (min^{-1})	$t_{1/2}$ (min)	R^2	k_{app} (min^{-1})	$t_{1/2}$ (min)	R^2
TiO_2	0.001874	368.20	99.03	0.005020	137.45	99.24	0.007861	87.77	99.52
1% CeO_2/TiO_2	0.001279	539.48	99.46	0.011200	61.61	99.39	0.011693	59.00	98.87
2% CeO_2/TiO_2	0.002529	272.83	99.19	0.009405	73.36	99.59	0.017291	39.90	99.11
3% CeO_2/TiO_2	0.002103	328.10	98.99	0.009935	69.45	98.61	0.009496	72.66	99.77
5% CeO_2/TiO_2	0.000289	2387.54	99.42	0.011518	59.91	99.00	0.017209	40.09	99.50
10% CeO_2/TiO_2	0.000440	1568.18	99.70	0.014848	46.47	99.41	0.021309	32.38	99.25

conduction band energy of TiO_2 3.26 eV compared to CeO_2 2.81 eV, these excited electrons migrate to the TiO_2 conduction band. Subsequently, they reduce surface oxygen, leading to the formation of reactive oxygen species, including superoxide ($\cdot O_2^-$) and hydroxyl ($\cdot$OOH/$\cdot$OH) radicals, on the CeO_2/TiO_2 surface. Simultaneously, the photoexcitation generates holes in the CeO_2 valence band. These holes, acting as strong oxidants, react with H_2O or HO^-, producing additional hydroxyl radicals [72,89]. These reactive oxygen species then degrade phenol, mineralizing it into CO_2 and H_2O through various intermediate products. The phenol degradation process over CeO_2/TiO_2 can be summarized as follows: when illuminated, the CeO_2/TiO_2 composite absorbs photons, resulting in the efficient separation of electrons and holes:

$$CeO_2/TiO_2 + h\lambda \rightarrow h^+(CeO_2) + e^-(TiO_2) \quad (5)$$

Holes interact with H_2O, generating hydroxyl radicals ($\cdot$OH), while electrons interact with H_2O_2, also producing $\cdot$OH [22,77,78].

$$h^+ + H_2O \rightarrow H^+ + \cdot OH \quad (6)$$

$$H_2O_2 + e^- \rightarrow OH^- + \cdot OH \quad (7)$$

Ce^{4+} ions capture electrons, becoming Ce^{3+}, and then react with adsorbed oxygen to form superoxide radicals ($\cdot O_2^-$) [83].

$$Ce^{4+} + e^- \rightarrow Ce^{3+} \quad (8)$$

$$Ce^{3+} + O_2 \rightarrow Ce^{+4} + \cdot O_2^- \quad (9)$$

The combined presence of $\cdot$OH and $\cdot O_2^-$ readily oxidizes phenol to CO_2, H_2O and intermediate products.

($\cdot$OH, $\cdot O_2^-$) + phenol → CO_2+H_2O+ intermediate products 10)

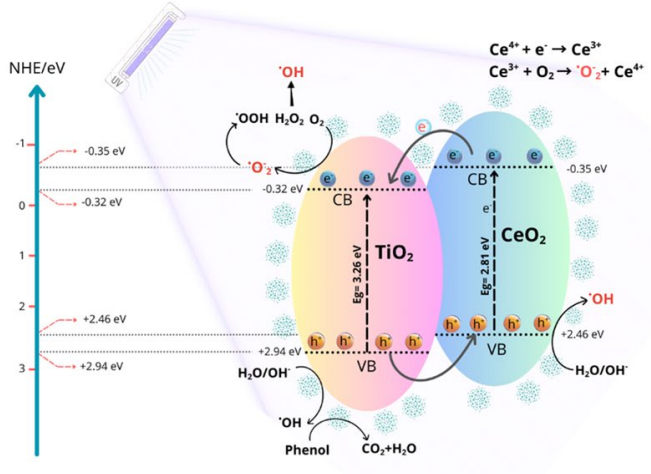

Figure 10. Photocatalytic mechanism of CeO_2/TiO_2.

Photocatalytic phenol degradation on 10 %CeO_2/TiO_2 with H_2O_2 was further studied under different conditions.

3.2.3 Effect of added H_2O_2 concentration on phenol photodegradation

Hydrogen peroxide (H_2O_2) dosage is critical in photo-Fenton-like reactions, as it generates hydroxyl radicals ($\cdot$OH), which are the primary oxidative species, by reacting with the catalyst surface. To determine the optimal dosage, 10 %CeO_2/TiO_2 was irradiated with varying H_2O_2 concentrations (0.4-3.6 mM) at pH of 7, a reaction temperature of 20 °C, and a catalyst dosage of 0.1 g in 130 mL of phenol solution (Figure 11). Initial increases in H_2O_2 (0.4-0.6 mM) led to a slight improvement in phenol removal efficiency, from 91.16 % to 99.05 %. However, further increases above 1.2 mM yielded negligible improvements and, as supported by previous studies [39,90,91], eventually decreased the degradation rate. This can be explained by two competing effects. First, increased H_2O_2 concentration initially enhances $\cdot$OH production, accelerating pollutant degradation ($H_2O_2 + h\nu \rightarrow 2\ \cdot$OH). Second, at

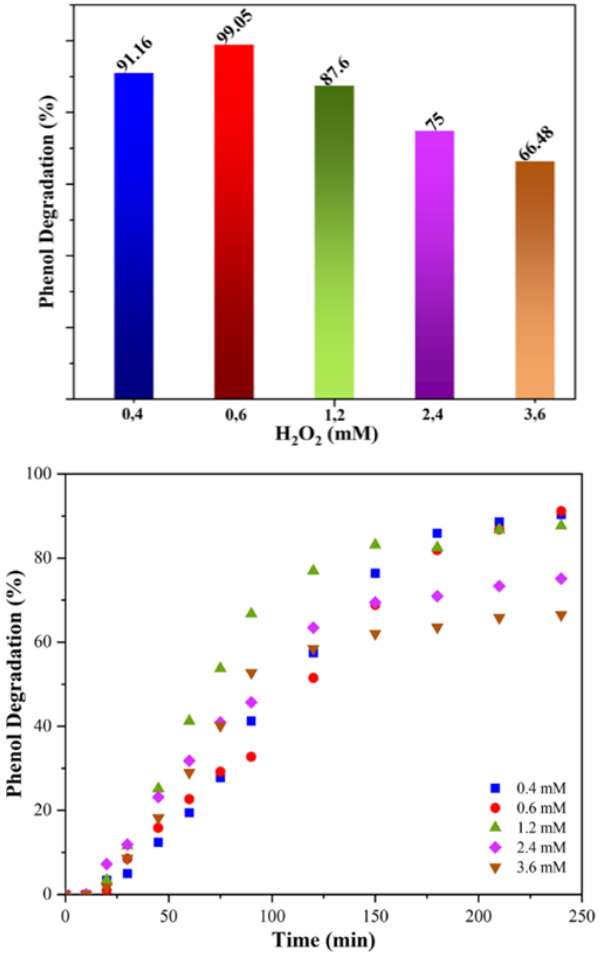

Figure 11. Effect of H_2O_2 concentration on the photocatalytic degradation of phenol (initial pH = 7, 25 °C, 0.1 g of catalyst, and 30 ppm phenol).

concentrations above 1.2 mM, excess •OH reacts with H_2O_2, forming less reactive hydroperoxyl radicals (HO_2•) (H_2O_2 + •OH → HO_2• + H_2O) [92,93].

Furthermore, hydroperoxyl radicals (HO_2•) can react with hydroxyl radicals (•OH), leading to the formation of water and oxygen (HO_2• + •OH → H_2O + O_2). Additionally, excess •OH can undergo recombination (•OH + •OH → H_2O_2), further diminishing the available •OH in the solution. This scavenging effect of •OH significantly reduces degradation efficiency. Therefore, the optimal H_2O_2 concentration for this experiment was found to be 0.6 mM [94].

3.2.4 Effect of initial pH

In the photocatalytic degradation of organic pollutants using semiconductor metal oxides, pH plays a crucial role as it influences the surface charge of the particles in solution [95]. This influence is primarily exerted through the alteration of the catalyst's surface charge; a phenomenon directly linked to the point of zero charge (pH_{pzc}). When the pH is below the pH_{pzc}, the surface becomes positively charged due to protonation, while above the pH_{pzc}, it becomes negatively charged due to deprotonation. The effect of pH on the photodegradation of phenol in the presence of 10 %CeO_2/TiO_2 particles was studied over a broad pH range, from 3 to 11, with a constant photocatalyst dosage of 0.1 g, a 0.6 mM dosage of H_2O_2, and an initial phenol concentration of 30 ppm (130 mL). The phenol degradation percentages obtained for pH values of 3, 4, 7, 8, and 11 were 28.44 %, 78.00 %, 91.16 %, 99.05 %, and 89.00 %, respectively (Figure 12). The results indicated that the photodegradation efficiency increased with pH up to 8 and then decreased. Lower photocatalytic degradation was observed when the phenol solution was either acidic or alkaline. Explaining the effect of pH on the photocatalytic process is a challenging task due to its multiple roles, such as electrostatic interactions between the semiconductor surface, solvent molecules, the substrate, and the charged radicals formed during the reaction process. The pH_{zpc} of 10%CeO_2/TiO_2 was found to be 6.54. When the pH was between 3 and 4, Cl^- ions from HCl could adsorb onto the catalyst surface, reducing phenol degradation. At neutral and slightly basic pH values, phenol exists primarily in its nonionic form, minimizing its water solubility and maximizing adsorption onto the catalyst. The charge attraction between the negatively charged phenol molecules and the positively charged catalyst particles enhances the coupling of phenol molecules with CeO_2/TiO_2 particles. On the other hand, at higher pH values, phenol tends to exist as phenolate ($C_6H_5O^-$) anions. These anions have extremely high solubility in solution and will not be significantly adsorbed. Coulombic repulsion between the negatively charged surface of the catalyst particles and the hydroxide anions can prevent the formation of hydroxyl radicals, thus reducing photodegradation. Additionally, the presence of OH^- can increase the number of •OH radicals, which are powerful oxidizers capable of rapidly decomposing phenol. The optimum pH was found to be 8. In this case, CeO_2/Ti-OH is stable, allowing the photocatalyst to efficiently capture the appropriate energy, making the photocatalytic process effective [96]. At acidic pH, the formation of •OH radicals are less compared to alkaline pH due to slower electron-hole formation [97]. The optimum pH is in the basic solution where the photocatalyst is negatively charged, and the phenol is positively charged, resulting in a favorable interaction. Under alkaline conditions, competitive adsorption of NaOH ions leads to lower phenol photocatalytic degradation [98]. In strongly alkaline

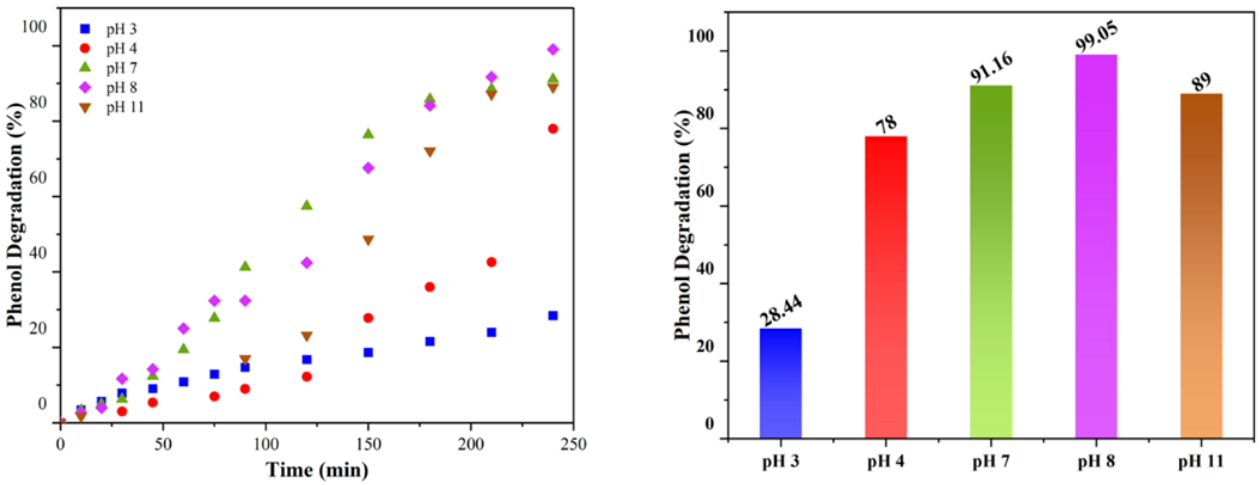

Figure 12. Effect of initial solution pH on the photocatalytic degradation of phenol (0.6 mM H_2O_2, 25 °C, 0.1 g of catalyst, and 30 ppm phenol).

environments, as the pH rises to 11, phenol adopts a negative charge. This, in conjunction with a reduced energy absorption capacity of the photocatalyst, leads to a repulsive interaction between the two [99,100].

3.2.5 Effect of photocatalyst dosage

Catalyst dosage is a critical factor in heterogeneous photocatalytic reactions. To assess its impact on CeO_2/TiO_2 the photodegradation of phenol, experiments were conducted by varying the amount from 0.025 g to 0.4 g (Figure 13), while maintaining the initial pH at 8, the phenol concentration at 30 ppm, and the reaction time at 240 minutes. The optimal degradation efficiency (99.05 %) was achieved with a 0.1 g catalyst dosage. This can be attributed to an adequate number of photocatalyst particles, which maximizes electron/hole pair generation, increases active sites, and promotes hydroxyl radical formation, thereby enhancing photodegradation. However, higher dosages (0.2 g and 0.4 g) led to reduced efficiency. This is likely due to catalyst coagulation, as reported by Mei *et al.* [90], which decreases active sites and hinders contact between the catalyst and H_2O_2. Additionally, excessive catalyst can reduce light transmittance and increase scattering, lowering electron/hole pair utilization. Specifically, an increase in the turbidity of the solution, caused by the excess catalyst, results in a reduction in the degree of light penetration [101]. Based on the experimental results, the optimal photocatalyst dosage was determined to be 0.1 g.

3.2.6 Effect of temperature

The impact of temperature on phenol removal was tested across a range of temperatures from 8 to 50 °C. The experiment was conducted at a pH of 8, using a 0.4 mM dosage of H_2O_2 and a 0.1 g dosage of catalyst and 30 ppm phenol solution. The phenol degradation efficiency as a function of temperature is illustrated in Figure 14. The results indicate that the rate of photocatalytic

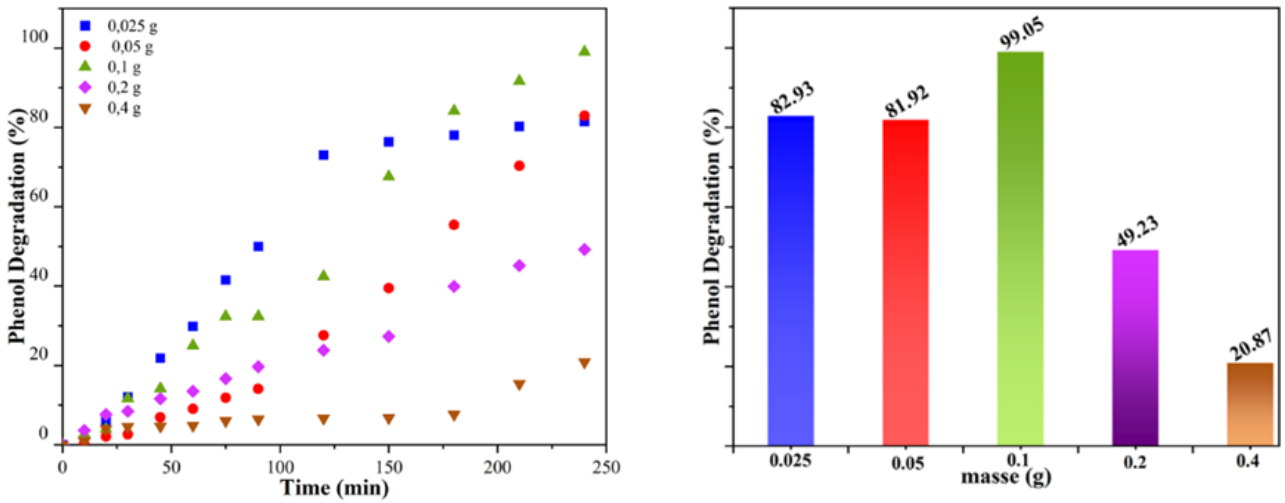

Figure 13. Effect of catalyst dosage (10 %CeO_2/TiO_2 on the photocatalytic degradation of phenol (initial pH = 8, 25 °C, 0.6 mM H_2O_2, at 30 ppm phenol).

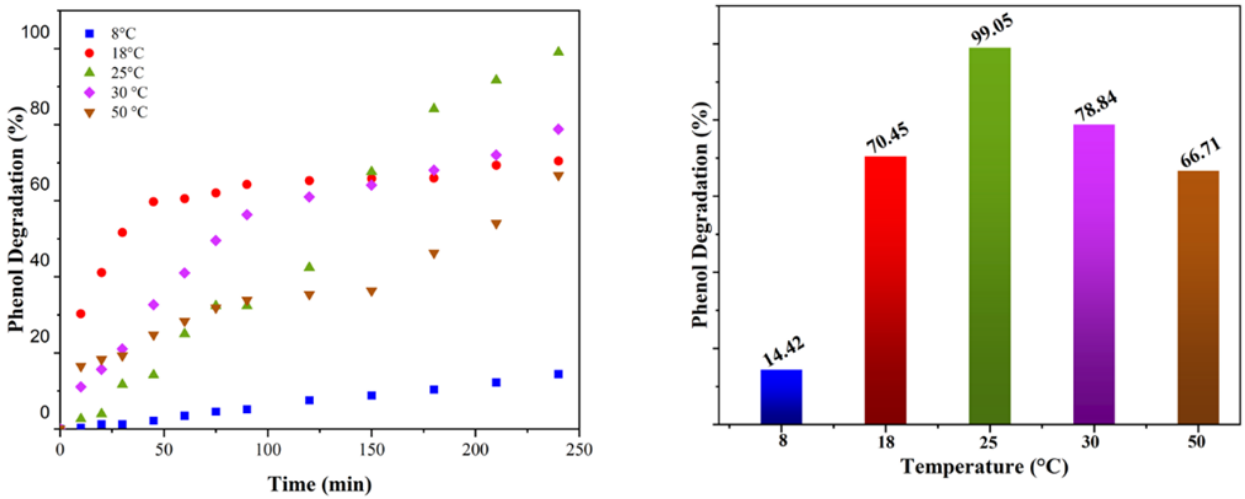

Figure 14. Impact of temperature variation on phenol photocatalytic degradation (initial pH of 8, 0.6 mM H_2O_2, 0.1 g of catalyst, and 30 ppm phenol).

degradation is temperature-dependent. The phenol removal rate increased as the temperature rose from 8 to 25 °C but declined at 30 and 50 °C. While temperature can generally enhance reaction kinetics and adsorption [102], excessive temperatures (>80 °C) lead to charge carrier recombination and reduced organic adsorption onto catalyst [103,104].

3.2.7 Effect of initial phenol concentration

A key parameter in water treatment is the initial pollutant concentration. To investigate this, phenol degradation was assessed at concentrations ranging from 15 to 60 ppm, under fixed conditions: pH of 8, 0.1 g of 10 % CeO_2/TiO_2, and a 240-minute reaction time (Figure 15). The highest degradation (99.05 %) occurred at 30 ppm. The observed decrease in degradation efficiency at higher initial concentrations (40-60 ppm), is attributed to the increased adsorption of phenol on CeO_2/TiO_2. This occupation of active sites restricts the adsorption of hydroxyl ions, leading to a reduction in hydroxyl radical generation. Furthermore, the increased phenol concentration in solution causes photons to be absorbed before reaching the catalyst, thereby decreasing photon absorption and the overall degradation rate [8,105,106].

3.2.8 The effect of the presence of radical scavengers

Photocatalytic oxidation relies on several key oxidative species: superoxide radicals ($\cdot O_2^-$), electrons (e^-), holes (h^+), and hydroxyl radicals ($\cdot OH$). To better understand the underlying photocatalytic mechanisms, experiments were conducted to identify these active species using specific scavengers. In this study, 0.8 mM solutions of p-benzonquinone (p-BQ) ($C_6H_4(=O)_2$, ≥ 98 %, Sigma-Aldrich), 2 mM silver nitrate ($AgNO_3$ > 99 %, Sigma-Aldrich), 2 mM disodium ethylenediaminetetraacetate (EDTA-2Na) ($C_{10}H_{14}N_2Na_2O_8 \cdot 2H_2O$, 97 %, Sigma-Aldrich), and 10 mM propan-2-ol (iso-proOH) ($(CH_3)_2CHOH$, ≥ 99.5 %, Sigma-Aldrich,) were introduced into the phenol solution to selectively scavenge $\cdot O_2^-$, e^-, h^+, and $\cdot OH$, respectively [107-110]. The resulting phenol degradation efficiencies after 240 minutes of UV irradiation with 10% CeO_2/TiO_2 are shown in Figure 16.

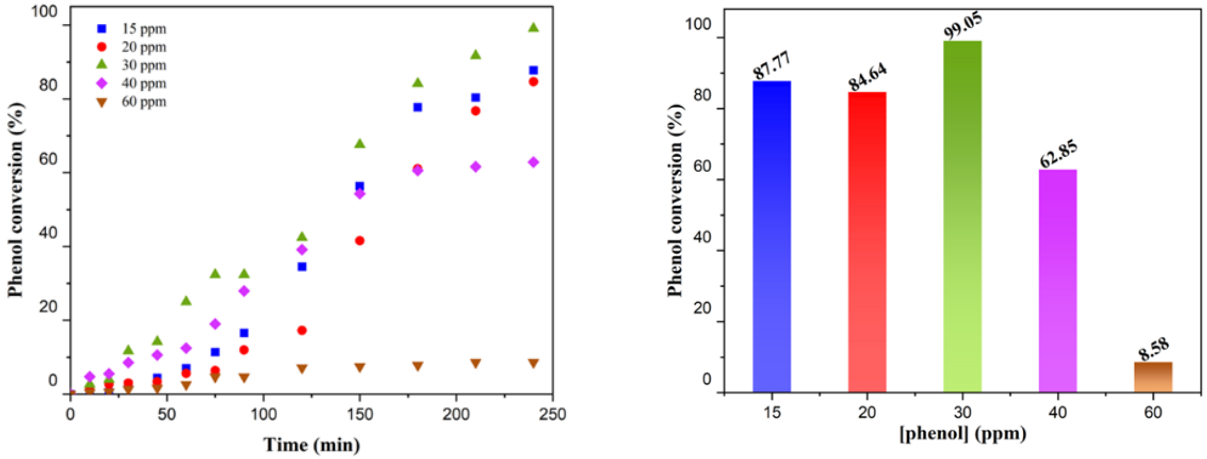

Figure 15. Influence of initial phenol concentration on photocatalytic degradation (initial pH = 8, 0.6 mM H_2O_2, 25 °C, 0.1 g of catalyst).

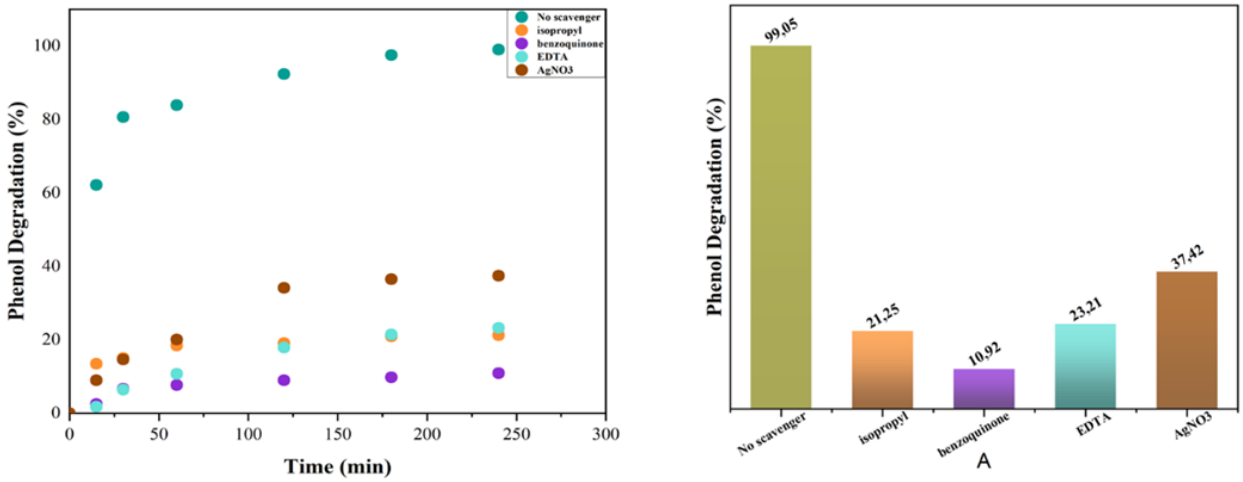

Figure 16. Effect of the presence of radical scavengers on photocatalytic degradation of phenol.

In the absence of scavengers, 99.05 % phenol degradation was observed. However, the addition of p-BQ, iso-proOH, EDTA-2Na, and $AgNO_3$ significantly reduced degradation to 10.92 %, 21.25 %, 23.21 %, and 37.42 %, respectively. These results indicate that superoxide radicals ($\bullet O_2^-$) are the dominant active species, followed by photogenerated electrons (e^-) and holes (h^+). Furthermore, the limited impact of iso-proOH suggests that hydroxyl radicals ($\bullet OH$) play a less significant role in this photocatalytic process.

3.3. Reusability

The stability of the 10%CeO_2/TiO_2 photocatalyst was evaluated over five successive experimental cycles employing a phenol solution with a concentration of 30 ppm, a pH of 8, 0.4 mM of H_2O_2, and 0.1 g of catalyst. Following each experiment, the photocatalyst was recovered via centrifugation, extensively rinsed with distilled water, and then dried at 80 °C for 12 hours. The reduction in phenol concentration for each cycle is depicted in Figure 17. The 10%CeO_2/TiO_2 photocatalyst exhibited a phenol degradation efficiency of approximately 92 % during the initial three cycles. A marginal decline in photocatalytic activity was noted in the fifth cycle, yielding a degradation rate of 88.01 %. The observed decrease in degradation percentage is potentially attributable to material loss during the recovery procedure. Moreover, the deactivation of the photocatalyst is likely associated with surface poisoning possibly induced by adsorbed intermediates [74]. These observations demonstrate that the 10 % CeO_2/TiO_2 photocatalyst can be effectively reused for a minimum of five cycles, thus validating its stability throughout the cyclic photocatalytic degradation of phenol.

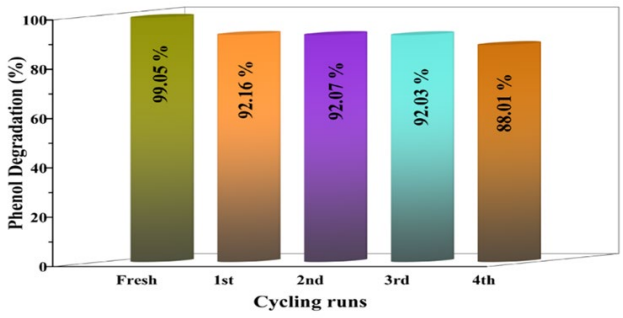

Figure 17. Cycling test of the 10%CeO_2/TiO_2 sample.

3.4 Comparative study

Table 4 summarizes recent studies on the catalytic activity of various materials for phenol degradation. The catalytic performances of the prepared catalysts CeO_2/TiO_2 are comparable to or exceed those reported in the literature. This suggests that these synthesized materials are promising candidates for removing toxic phenol pollutants

4. Conclusions

In conclusion, x% CeO_2/TiO_2 (x = 1, 2, 3, 5 and 10) photocatalytic materials were successfully prepared by the wetness impregnation method and characterized using XRD, FTIR, surface area and pore volume measurements, Raman spectroscopy, SEM, and UV-Vis-DRS. Their effectiveness in degrading phenol in aqueous solutions under UV irradiation (λ = 254 nm) was compared across various oxidation processes. The photocatalyst/UV/H_2O_2 system demonstrated significantly higher efficiency than photocatalyst/UV or photocatalyst/H_2O_2 alone, with the degradation rate following the order: photocatalyst/H_2O_2 < photocatalyst/UV < photocatalyst/UV/H_2O_2. Among the synthesized materials, 10% CeO_2/TiO_2 catalyst showed superior degradation efficiency of 99.05 %, in heterogeneous photo-Fenton process and maintained at 88.01 % after five cycles. The oxidation rate was influenced by many factors, such as photocatalyst dosage, initial pH, phenol concentration, H_2O_2 volume, and temperature.

Table 4. Comparison of various catalysts for phenol degradation.

Material	Experimental conditions		Reaction Time (min)	Degradation (%)	References
	[Catalyst] (g/L)	[Phenol] (mg/L)			
Anatase TiO_2 nanosheets	1.0	50	350	94.23	[2]
TiO_2/Pumice	50	11.2	240	90	[22]
Nanostructured CeO_2	1.3	50	180	35	[23]
CeO_2/TiO_2 heterostructures	0.5	38	120	99.1	[43]
TiO_2/ZnO	50	50	360	99.51	[57]
γ-Cu-Ce-Al_2O_3	0.8	100	120	95	[90]
TiO_2/SiO_2	0.2	10	270	64.95	[107]
10 %CeO_2/TiO_2	0.1	30	240	99.05	Current work

Optimal conditions for maximum degradation (99.05 %) were: 0.1 g catalyst, 0.6 mM hydrogen peroxide, 25 °C reaction temperature, initial pH of 8, 30 ppm initial phenol concentration, and 240 minutes reaction time. The free radical trapping experiments indicate that photogenerated superoxide radicals ($\bullet O_2^-$) are the primary active species for phenol photocatalytic degradation, followed by photogenerated electrons (e^-) and holes (h^+), while hydroxyl radicals ($\bullet OH$) played a less significant role.

Acknowledgment

This work was supported by the Algerian Ministry of Higher Education and Scientific Research, the General Direction for Scientific and Technological Research (DGRST), and the Thematic Research Agency for Science and Technology (ATRST).

CRedit Author Statement

Author Contributions: Farah Guitouni: Conceptualization, Data Curation; Formal analysis, Investigation, Methodology, Supervision; Ilhem Rekkab-Hammoumraoui: Conceptualization, Supervision, Writing – Reviewing and Editing; Sanaa EL Korso: Conceptualization, Methodology, Supervision, Formal analysis, Mohamed Sassi: Supervision, Formal analysis; Chewki Ziani-Cherif: Funding acquisition, Project administration, Supervision, Validation. All authors have read and agreed to the published version of the manuscript.

References

[1] Prabha, I., Lathasree, S. (2014). Photodegradation of phenol by zinc oxide, titania and zinc oxide–titania composites: Nanoparticle synthesis, characterization and comparative photocatalytic efficiencies. *Materials Science in Semiconductor Processing*, 26, 603-613. DOI: 10.1016/j.mssp.2014.05.031.

[2] Zulfiqar, M., Sufian, S., Rabat, N.E., Mansor, N. (2020). Photocatalytic degradation and adsorption of phenol by solvent-controlled TiO_2 nanosheets assisted with H_2O_2 and $FeCl_3$: Kinetic, isotherm and thermodynamic analysis. *Journal of Molecular Liquids*. 308, 112941. DOI: 10.1016/j.molliq.2020.112941.

[3] Zamri, M.S.F.A., Sapawe, N., (2018). Performance studies of electrobiosynthesis of titanium dioxide nanoparticles (TiO_2) for phenol degradation. *Materials Today: Proceedings*. 5, 21797-21801. DOI: 10.1016/j.matpr.2018.07.034.

[4] Huang, L., Li, D., Liu, J., Yang, L., Dai, C., Ren, N., Feng, Y., (2020). Construction of TiO2 nanotube clusters on Ti mesh for immobilizing Sb-SnO_2 to boost electrocatalytic phenol degradation. *Journal of Hazardous Materials*. 393, 122329. DOI: 10.1016/j.jhazmat.2020.122329.

[5] Aghda, S.M.F., Samadi, A., Asadollahfardi, G., Dastafkan, F., (2023). Sustainable rural development based on groundwater quality using fuzzy logic and gis. a case study: *Maku, Iran. Environmental Engineering Management Journal*. 22. DOI: 10.30638/eemj.2023.005.

[6] Vaiano, V., Matarangolo, M., Murcia, J., Rojas, H., Navio, J.A., Hidalgo, M., (2018). Enhanced photocatalytic removal of phenol from aqueous solutions using ZnO modified with Ag. *Applied Catalysis B: Environmental*. 225, 197-206. DOI: 10.1016/j.apcatb.2017.11.075.

[7] Mohd, A., (2022). Presence of phenol in wastewater effluent and its removal: an overview. International *Journal of Environmental Analytical Chemistry*. 102, 1362-1384. DOI: 10.1080/03067319.2020.1738412.

[8] Broccoli, F., Paparo, R., Iesce, M.R., Di Serio, M., Russo, V. (2023). Heterogeneous Photodegradation Reaction of Phenol Promoted by TiO_2: A Kinetic Study. *ChemEngineering*. 7, 27. DOI: 10.3390/chemengineering7020027.

[9] Wardhani, S., Purwonugroho, D., Fitri, C.W., Prananto, Y.P. (2018). Effect of pH and irradiation time on TiO_2-chitosan activity for phenol photo-degradation. In *AIP Publishing* LLC, pp. 050009. DOI: 10.1063/1.5062759

[10] Yuting, F., Changbo, L., Guozheng, Z., Hui, L., Shuo, W., Hongzhu, X., (2021). Progress in treatment technology of phenol-containing industrial wastewater. *IOP Conference Series: Earth and Environmental Science*. 787, 012054. DOI: 10.1088/1755-1315/787/1/012054.

[11] Devendrapandi, G., Balu, R., Ayyappan, K., Ayyamperumal, R., Alhammadi, S., Lavanya, M., Senthilkumar, R., Karthika, P., (2024). Unearthing Earth's secrets: Exploring the environmental legacy of contaminants in soil, water, and sediments. *Environmental Research*. 249, 118246. DOI: 10.1016/j.envres.2024.118246.

[12] Ma, J., Wang, Y., Zhang, Z., Wang, X., Hou, X., Hu, Q. (2024). Conventional and toxic pollutants removal of toxic herbal wastewater by using moving bed biofilm reactor, coagulation, and adsorption. *Journal of Environmental Chemical Engineering*. 12, 112705. DOI: 10.1016/j.jece.2024.112705.

[13] Zhang, S., An, Z., Su, X., Hou, A., Liu, L., Zhang, L., He, Q., Sun, F., Lei, Z., Lin, H., Lai, J. (2023). Phenol degradation at high salinity by a resuscitated strain Pseudomonas sp. SAS26: kinetics and pathway. *Journal of Environmental Chemical Engineering*. 11, 110182. DOI: 10.1016/j.jece.2023.110182.

[14] Vaez, Z., Javanbakht, V. (2020). Synthesis, characterization and photocatalytic activity of ZSM-5/ZnO nanocomposite modified by Ag nanoparticles for methyl orange degradation. *Journal of Photochemistry Photobiology A: Chemistry*. 388, 112064. DOI: 10.1016/j.jphotochem.2019.112064.

[15] Khataee, A., Pons, M-N. Zahraa, O., (2009). Photocatalytic degradation of three azo dyes using immobilized TiO_2 nanoparticles on glass plates activated by UV light irradiation: Influence of dye molecular structure. *Journal of Hazardous Materials*. 168, 451-457. DOI: 10.1016/j.jhazmat.2009.02.052.

[16] Sinar Mashuri, S.I., Ibrahim, M.L., Kasim, M.F., Mastuli, M.S., Rashid, U., Abdullah, A.H., Islam, A., Asikin Mijan, N., Tan, Y.H., Mansir, N. (2020). Photocatalysis for Organic Wastewater Treatment: From the Basis to Current Challenges for Society. *Catalysts*. 10, 1260. DOI: 10.3390/catal10111260.

[17] Mahgoub, S.A., Qattan, S.Y., Salem, S.S., Abdelbasit, H.M., Raafat, M., Ashkan, M.F., Al-Quwaie, D.A., Motwali, E.A., Alqahtani, F.S., Abd El-Fattah, H.I. (2023). Characterization and Biodegradation of Phenol by Pseudomonas aeruginosa and Klebsiella variicola Strains Isolated from Sewage Sludge and Their Effect on Soybean Seeds Germination. *Molecules*. 28, 1203. DOI: 10.3390/molecules28031203.

[18] Babaei, A.A., Golshan, M., Kakavandi, B. (2021). A heterogeneous photocatalytic sulfate radical-based oxidation process for efficient degradation of 4-chlorophenol using TiO_2 anchored on Fe oxides@carbon. *Process Safety Environmental Protection*. 149, 35-47. DOI: 10.1016/j.psep.2020.10.028.

[19] Bashiri, F., Khezri, S.M., Kalantary, R.R., Kakavandi, B. (2020). Enhanced photocatalytic degradation of metronidazole by TiO_2 decorated on magnetic reduced graphene oxide: Characterization, optimization and reaction mechanism studies. *Journal of Molecular Liquids*. 314, 113608. DOI: 10.1016/j.molliq.2020.113608.

[20] Zhang, T., Liu, Y., Rao, Y., Li, X., Yuan, D., Tang, S., Zhao, Q., (2020). Enhanced photocatalytic activity of TiO_2 with acetylene black and persulfate for degradation of tetracycline hydrochloride under visible light. *Chemical Engineering Journal*. 384, 123350. DOI: 10.1016/j.cej.2019.123350.

[21] Rahman, Z.U., Wei, N., Feng, M., Wang, D. (2019). TiO_2 hollow spheres with separated Au and RuO_2 co-catalysts for efficient photocatalytic water splitting. *International Journal of Hydrogen Energy*. 44, 13221-13231. DOI: 10.1016/j.ijhydene.2019.03.176.

[22] Ratnawati, R., Enjarlis, E., Yuli, A.H., Marcelinus, C., Slamet, S. (2020). Degradation of Phenol in Pharmaceutical Wastewater using TiO_2/Pumice and O_3/Active Carbon. *Bulletin of Chemical Reaction Engineering & Catalysis*, 15 (1) 2020, 146-154. DOI: 10.9767/bcrec.15.1.4432.146-154

[23] Aslam, M., Qamar, M., Soomro, M.T., Ismail, I.M., Salah, N., Almeelbi, T., Gondal, M., Hameed, A. (2016). The effect of sunlight induced surface defects on the photocatalytic activity of nanosized CeO_2 for the degradation of phenol and its derivatives. *Applied Catalysis B: Environmental*. 180, 391-402. DOI: 10.1016/j.apcatb.2015.06.050.

[24] Abdullah, H., Khan, M.R., Pudukudy, M., Yaakob, Z., Ismail, N.A. (2015). CeO_2-TiO_2 as a visible light active catalyst for the photoreduction of CO_2 to methanol. *Journal of Rare Earths*. 33, 1155-1161. DOI: 10.1016/S1002-0721(14)60540-8.

[25] Montini, T., Melchionna, M., Monai, M., Fornasiero, P. (2016). Fundamentals and Catalytic Applications of CeO_2-Based Materials. *Chemical Reviews*. 116, 5987-6041. DOI: 10.1021/acs.chemrev.5b00603.

[26] Konsolakis, M., (2016). The role of Copper–Ceria interactions in catalysis science: Recent theoretical and experimental advances. *Applied Catalysis B: Environmental*. 198, 49-66. DOI: 10.1016/j.apcatb.2016.05.037.

[27] Konsolakis, M., Lykaki, M. (2020). Recent Advances on the Rational Design of Non-Precious Metal Oxide Catalysts Exemplified by CuO_x/CeO_2 Binary System: Implications of Size, Shape and Electronic Effects on Intrinsic Reactivity and Metal-Support Interactions. *Catalysts*. 10, 160. DOI: 10.3390/catal10020160.

[28] Melchionna, M., Fornasiero, P. (2014). The role of ceria-based nanostructured materials in energy applications. *Materials Today*. 17, 349-357. DOI: 10.1016/j.mattod.2014.05.005.

[29] Tang, W.-X., Gao, P.-X. (2016). Nanostructured cerium oxide: preparation, characterization, and application in energy and environmental catalysis. *MRS Communications*. 6, 311-329. DOI: 10.1557/mrc.2016.52.

[30] Corberan, V.C., Rives, V., Stathopoulos, V. (2019). Recent applications of nanometal oxide catalysts in oxidation reactions. In *Advanced Nanomaterials for Catalysis and Energy*, (Elsevier), 227-293. DOI: 10.1016/B978-0-12-814807-5.00007-3.

[31] Paier, J., Penschke, C., Sauer, J. (2013). Oxygen Defects and Surface Chemistry of Ceria: Quantum Chemical Studies Compared to Experiment. *Chemical Reviews*. 113, 3949-3985. DOI: 10.1021/cr3004949

[32] Zhang, H., Wang, J. (2017). Catalytic Ozonation of Humic Acids by Ce–Ti Composite Catalysts. *Kinetics and Catalysis*. 58, 734-740. DOI: 10.1134/S0023158417060167

[33] Siriwong, C., Wetchakun, N., Inceesungvorn, B., Channei, D., Samerjai, T., Phanichphant, S. (2012). Doped-metal oxide nanoparticles for use as photocatalysts. *Progress in Crystal Growth and Characterization of Materials*. 58, 145-163. DOI: 10.1016/j.pcrysgrow.2012.02.004.

[34] Tian, J., Sang, Y., Zhao, Z., Zhou, W., Wang, D., Kang, X., Liu, H., Wang, J., Chen, S., Cai, H. (2013). Enhanced Photocatalytic Performances of CeO_2/TiO_2 Nanobelt Heterostructures. *Small*. 9, 3864-3872. DOI: 10.1002/smll.201202346

[35] Ameen, S., Shaheer Akhtar, M., Seo, H-K., Shin, H-S. (2014). Solution-processed CeO_2/TiO_2 nanocomposite as potent visible light photocatalyst for the degradation of bromophenol dye. *Chemical Engineering Journal*. 247, 193-198. DOI: 10.1016/j.cej.2014.02.104

[36] Cano-Franco, J.C., Alvarez-Lainez, M. (2019). Effect of CeO_2 content in morphology and optoelectronic properties of TiO_2-CeO_2 nanoparticles in visible light organic degradation. *Materials Science in Semiconductor Processing*. 90, 190-197. DOI: 10.1016/j.mssp.2018.10.017.

[37] Pudukudy, M., Jia, Q., Yuan, J., Megala, S., Rajendran, R., Shan, S. (2020). Influence of CeO_2 loading on the structural, textural, optical and photocatalytic properties of single-pot sol-gel derived ultrafine CeO_2/TiO_2 nanocomposites for the efficient degradation of tetracycline under visible light irradiation. *Materials Science in Semiconductor Processing*. 108, 104891. DOI: 10.1016/j.mssp.2019.104891.

[38] Jun, L., Wang, L-l., Fei, Z-Y., Xian, C., Tang, J-H., Cui, M-F., Xu, Q. (2016). Structure and properties of amorphous CeO_2@TiO_2 catalyst and its performance in the selective catalytic reduction of NO with NH3. *Journal of Fuel Chemistry Technology*. 44, 954-960. DOI: 10.1016/S1872-5813(16)30043-3.

[39] Mukhlish, M.Z.B., Islam, M.A., Rahman, M.A., Hossain, S., Islam, M.A., Uddin, M.T. (2021). Facile solid-state synthesis of heterojunction CeO_2/TiO_2 nanocomposite as an efficient photocatalyst for the degradation of organic pollutants. *Desalination Water Treatment*. 230, 169-183. DOI: 10.5004/dwt.2021.27416.

[40] Nasir, M., Xi, Z., Xing, M., Zhang, J., Chen, F., Tian, B., Bagwasi, S. (2013). Study of Synergistic Effect of Ce- and S-Codoping on the Enhancement of Visible-Light Photocatalytic Activity of TiO_2. *The Journal of Physical Chemistry: C*, 117, 9520-9528. DOI: 10.1021/jp402575w.

[41] Gao, X., Jiang, Y., Fu, Y., Zhong, Y., Luo, Z., Cen, K. (2010). Preparation and characterization of CeO_2/TiO_2 catalysts for selective catalytic reduction of NO with NH_3. *Catalysis Communications*. 11, 465-469. DOI: 10.1016/j.catcom.2009.11.024.

[42] Fang, J., Bi, X., Si, D., Jiang, Z., Huang, W. (2007). Spectroscopic studies of interfacial structures of CeO_2–TiO_2 mixed oxides. *Applied Surface Science*, 253, 8952-8961. DOI: 10.1016/j.apsusc.2007.05.013.

[43] Wang, X., Xu, H., Luo, X., Li, M., Dai, M., Chen, Q., Song, H. (2021). Enhanced photocatalytic properties of CeO_2/TiO_2 heterostructures for phenol degradation. *Colloid and Interface Science Communications*. 44, 100476. DOI: 10.1016/j.colcom.2021.100476.

[44] Priyanka, K., Tresa, S. A., Jaseentha, O., Varghese, T. (2013). Cerium doped nanotitania-extended spectral response for enhanced photocatalysis. *Materials Research Express*. 1, 015003. DOI: 10.1088/2053-1591/1/1/015003.

[45] Rouquerol, F., Rouquerol, J., Sing, K. (1999). CHAPTER 2 - Thermodynamics of Adsorption at the Gas–Solid Interface. In *Adsorption by Powders and Porous Solids*, Rouquerol, F., Rouquerol, J., Sing, K. eds. (Academic Press), 27-50. DOI: 10.1016/B978-012598920-6/50003-8.

[46] Xu, W., Yu, Y., Zhang, C., He, H. (2008). Selective catalytic reduction of NO by NH_3 over a Ce/TiO_2 catalyst. *Catalysis Communications*. 9, 1453-1457. DOI: 10.1016/j.catcom.2007.12.012.

[47] Al-Hamdi, A.M., Sillanpaa, M., Dutta, J. (2016). Intermediate formation during photodegradation of phenol using lanthanum doped tin dioxide nanoparticles. *Research on Chemical Intermediates*. 42, 3055-3069. DOI: 10.1007/s11164-015-2197-9.

[48] Xiang, Q., Yu, J., Wang, W., Jaroniec, M. (2011). Nitrogen self-doped nanosized TiO_2 sheets with exposed {001} facets for enhanced visible-light photocatalytic activity. *Chemical Communications*. 47, 6906-6908. DOI: 10.1039/C1CC11740H.

[49] Wang, T., Sun, D.-C. (2008). Preparation and characterization of nanometer-scale powders ceria by electrochemical deposition method. *Materials Research Bulletin*. 43, 1754-1760. DOI: 10.1016/j.materresbull.2007.07.008.

[50] Andreescu, D., Matijevic, E., Goia, D.V. (2006). Formation of uniform colloidal ceria in polyol. *Colloids Surfaces A: Physicochemical Engineering Aspects*. 291, 93-100. DOI: 10.1016/j.colsurfa.2006.05.006.

[51] Liu, J., Zhao, Z., Wang, J., Xu, C., Duan, A., Jiang, G., Yang, Q. (2008). The highly active catalysts of nanometric CeO_2-supported cobalt oxides for soot combustion. *Applied Catalysis B: Environmental*. 84, 185-195. DOI: 10.1016/j.apcatb.2008.03.017.

[52] McDevitt, N.T., Baun, W.L. (1964). Infrared absorption study of metal oxides in the low frequency region (700-240 cm^{-1}). *Spectrochimica Acta*. 20, 799-808. DOI: 10.1016/0371-1951(64)80079-5.

[53] Larbot, A., Laaziz, I., Marignan, J., Quinson, J. (1992). Porous texture of a titanium oxide gel: evolution as a function of medium used. *Journal of Non-crystalline Solids*. 147, 157-161. DOI: 10.1016/S0022-3093(05)80610-6.

[54] Chhor, K., Bocquet, J., Pommier, C., (1992). Syntheses of submicron TiO_2 powders in vapor, liquid and supercritical phases, a comparative study. *Materials Chemistry Physics*. 32, 249-254. DOI: 10.1016/0254-0584(92)90207-O.

[55] Ouidri, S., Khalaf, H. (2009). Synthesis of benzaldehyde from toluene by a photocatalytic oxidation using TiO_2-pillared clays. *Journal of PhotochemistryPhotobiology A: Chemistry*. 207, 268-273. DOI: 10.1016/j.jphotochem.2009.07.019.

[56] Dali, A., Rekkab-Hammoumraoui, I., Choukchou-Braham, A., Bachir, R. (2015). Allylic oxidation of cyclohexene over ruthenium-doped titanium-pillared clay. *RSC Advances*. 5, 29167-29178. DOI: 10.1039/C4RA17129B.

[57] Kurniawan, Y.S., Yuliati, L. (2021). Activity Enhancement of P25 Titanium Dioxide by Zinc Oxide for Photocatalytic Phenol Degradation. *Bulletin of Chemical Reaction Engineering & Catalysis*, 16 (2), 310-319. DOI: 10.9767/bcrec.16.2.10319.310-319

[58] Maciel, C.G., de Freitas Silva, T., Hirooka, M.I., Belgacem, M.N., Assaf, J.M. (2012). Effect of nature of ceria support in CuO/CeO_2 catalyst for PROX-CO reaction. *Fuel*. 97, 245-252. DOI: 10.1016/j.fuel.2012.02.004.

[59] Deus, R., Cilense, M., Foschini, C., Ramirez, M., Longo, E., Simoes, A. (2013). Influence of mineralizer agents on the growth of crystalline CeO_2 nanospheres by the microwave-hydrothermal method. *Journal of Alloys Compounds*. 550, 245-251. DOI: 10.1016/j.jallcom.2012.10.001.

[60] Ohsaka, T., Izumi, F., Fujiki, Y. (1978). Raman spectrum of anatase, TiO_2. *Journal of Raman Spectroscopy*. 7, 321-324. DOI: 10.1002/jrs.1250070606.

[61] Ohsaka, T. (1980). Temperature Dependence of the Raman Spectrum in Anatase TiO_2. *Journal of the Physical Society of Japan*. 48, 1661-1668. DOI: 10.1143/JPSJ.48.1661.

[62] Coloon, G., Pijolat, M., Valdivieso, F., Vidal, H., Kaspar, J., Finocchio, E., Daturi, M., Pijolat, M., Valdivieso, F., Vidal, H., Kaspar, J., Finocchio, E., Daturi, M., Binet, J. C., Lavalley, J. T., Baker, R., Bernal, S. (1998). Surface and structural characterization of $Ce_xZr_{1-x}O_2$ CEZIRENCAT mixed oxides as potential three-way catalyst promoters. *Journal of the Chemical Society, Faraday Transactions*. 94, 3717-3726. DOI: 10.1039/A807680D.

[63] Weber, W., Hass, K., McBride, J. (1993). Raman study of CeO_2: Second-order scattering, lattice dynamics, and particle-size effects. *Physical Review B*. 48, 178. DOI: 10.1103/PhysRevB.48.178.

[64] Dhanalakshmi, J., Iyyapushpam, S., Nishanthi, S., Malligavathy, M., Padiyan, D.P. (2017). Investigation of oxygen vacancies in Ce coupled TiO_2 nanocomposites by Raman and PL spectra. *Advances in Natural Sciences: Nanoscience Nanotechnology*. 8, 015015. DOI: 10.1088/2043-6254/aa5984.

[65] Ding, J., Zhong, Q., Zhang, S. (2015); A New Insight into Catalytic Ozonation with Nanosized Ce–Ti Oxides for NO_x Removal: Confirmation of Ce–O–Ti for Active Sites. *Industrial Engineering Chemistry Research*. 54, 2012-2022. DOI: 10.1021/ie504100b.

[66] Tian, F., Zhang, Y., Zhang, J., Pan, C., (2012). Raman Spectroscopy: A New Approach to Measure the Percentage of Anatase TiO_2 Exposed (001) Facets. *The Journal of Physical Chemistry C*, 116, 7515-7519. DOI: 10.1021/jp301256h.

[67] Santara, B., Pal, B., Giri, P. (2011). Signature of strong ferromagnetism and optical properties of Co doped TiO_2 nanoparticles. *Journal of Applied Physics*. 110, 114322-113101. DOI: 10.1063/1.3665883.

[68] Ghasemi, S., Rahimnejad, S., Setayesh, S.R., Rohani, S., Gholami, M. (2009). Transition metal ions effect on the properties and photocatalytic activity of nanocrystalline TiO_2 prepared in an ionic liquid. *Journal of Hazardous Materials*. 172, 1573-1578. DOI: 10.1016/j.jhazmat.2009.08.029.

[69] Jiang, B., Zhang, S., Guo, X., Jin, B., Tian, Y. (2009). Preparation and photocatalytic activity of CeO_2/TiO_2 interface composite film. *Applied Surface Science*. 255, 5975-5978. DOI: 10.1016/j.apsusc.2009.01.049.

[70] Xu, Y-H., Zeng, Z-X. (2008). The preparation, characterization, and photocatalytic activities of $Ce\text{-}TiO_2/SiO_2$. *Journal of Molecular Catalysis A: Chemical*. 279, 77-81. DOI: 10.1016/j.molcata.2007.09.016.

[71] Li, W., Ma, Q., Wang, X., Chu, X-S., Wang, F., Wang, X-C., Wang, C-Y. (2020). Enhanced photoresponse and fast charge transfer: three-dimensional macroporous $g\text{-}C_3N_4/GO\text{-}TiO_2$ nanostructure for hydrogen evolution. *Journal of Materials Chemistry A*. 8, 19533-19543. DOI: 10.1039/D0TA07178A.

[72] Tomova, D., Iliev, V., Eliyas, A., Rakovsky, S. (2015). Promoting the oxidative removal rate of oxalic acid on gold-doped CeO_2/TiO_2 photocatalysts under UV and visible light irradiation. *Separation Purification Technology*. 156, 715-723. DOI: 10.1016/j.seppur.2015.10.070.

[73] Hashmi, S., Batalha, G.F., Van Tyne, C.J., Yilbas, B.S. (2014). Comprehensive Materials Processing (Elsevier).4, 187-200. DOI: 10.1016/B978-0-08-096532-1.00410-6

[74] Hadjltaief, H.B., Zina, M.B., Galvez, M.E., Da Costa, P., (2016). Photocatalytic degradation of methyl green dye in aqueous solution over natural clay-supported $ZnO–TiO_2$ catalysts. *Journal of Photochemistry Photobiology A: Chemistry*. 315, 25-33. DOI: 10.1016/j.jphotochem.2015.09.008.

[75] Jeong, M.-G., Park, E.J., Seo, H.O., Kim, K.-D., Kim, Y.D., Lim, D.C. (2013). Humidity effect on photocatalytic activity of TiO_2 and regeneration of deactivated photocatalysts. *Applied Surface Science*. 271, 164-170. DOI: 10.1016/j.apsusc.2013.01.155.

[76] Wang, J., Liu, X., Li, R., Qiao, P., Xiao, L., Fan, J. (2012). TiO_2 nanoparticles with increased surface hydroxyl groups and their improved photocatalytic activity. *Catalysis Communications*. 19, 96-99. DOI: 10.1016/j.catcom.2011.12.028.

[77] Zhang, J., Zhao, D., Wang, J., Yang, L. (2009). Photocatalytic oxidation of dibenzothiophene using TiO_2/bamboo charcoal. *Journal of Materials Science*. 44, 3112-3117. DOI: 10.1007/s10853-009-3413-z.

[78] Wang, C., Zhu, W., Xu, Y., Xu, H., Zhang, M., Chao, Y., Yin, S., Li, H., Wang, J. (2014). Preparation of TiO_2/g-C_3N_4 composites and their application in photocatalytic oxidative desulfurization. *Ceramics International*, 40, 11627-11635. DOI: 10.1016/j.ceramint.2014.03.156.

[79] Rani, S., Roy, S.C., Paulose, M., Varghese, O.K., Mor, G.K., Kim, S., Yoriya, S., LaTempa, T.J., Grimes, C. (2010). Synthesis and applications of electrochemically self-assembled titanianantube arrays. *Physical Chemistry Chemical Physics*. 12, 2780-2800. DOI: 10.1039/B924125F.

[80] Tian, J., Zhao, Z., Kumar, A., Boughton, R.I., Liu, H. (2014). Recent progress in design, synthesis, and applications of one-dimensional TiO_2 nanostructured surface heterostructures: a review. *Chemical Society Reviews*. 43, 6920-6937. DOI: 10.1039/C4CS00180J.

[81] Nolan, M., Fearon, J.E., Watson, G.W. (2006). Oxygen vacancy formation and migration in ceria. *Solid State Ionics*. 177, 3069-3074. DOI: 10.1016/j.ssi.2006.07.045.

[82] Xue, W., Zhang, G., Xu, X., Yang, X., Liu, C., Xu, Y. (2011). Preparation of titania nanotubes doped with cerium and their photocatalytic activity for glyphosate. *Chemical Engineering Journal*. 167, 397-402. DOI: 10.1016/j.cej.2011.01.007.

[83] Choudhury, B., Chetri, P., Choudhury, A. (2014). Oxygen defects and formation of Ce^{3+} affecting the photocatalytic performance of CeO_2 nanoparticles. *RSC Advances*. 4, 4663-4671. DOI: 10.1039/C3RA44603D.

[84] Park, H., Kim, H-I., Moon, G-H., Choi, W. (2016). Photoinduced charge transfer processes in solar photocatalysis based on modified TiO_2. *Energy Environmental Science and Pollution Research*. 9, 411-433. DOI: 10.1039/C5EE02575C.

[85] Belver, C., Bedia, J., Rodriguez, J. (2015), Titania–clay heterostructures with solar photocatalytic applications. *Applied Catalysis B: Environmental*. 176, 278-287. DOI: 10.1016/j.apcatb.2015.04.004.

[86] Elidrissi, B., Addou, M., Regragui, M., Monty, C., Bougrine, A., Kachouane, A. (2000). Structural and optical properties of CeO_2 thin films prepared by spray pyrolysis. *Thin Solid Films*. 379, 23-27. DOI: 10.1016/S0040-6090(00)01404-8.

[87] Zheng, S-Y., Andersson-Faldt, A., Stjerna, B., Granqvist, C. (1993). Optical properties of sputter-deposited cerium oxyfluoride thin films. *Applied Optics*. 32, 6303-6309. DOI: 10.1364/AO.32.006303.

[88] Hao, C., Li, J., Zhang, Z., Ji, Y., Zhan, H., Xiao, F., Wang, D., Liu, B., Su, F. (2015). Enhancement of photocatalytic properties of TiO_2 nanoparticles doped with CeO_2 and supported on SiO_2 for phenol degradation. *Applied Surface Science*. 331, 17-26. DOI: 10.1016/j.apsusc.2015.01.069.

[89] Lu, X., Li, X., Qian, J., Miao, N., Yao, C., Chen, Z. (2016). Synthesis and characterization of CeO_2/TiO_2 nanotube arrays and enhanced photocatalytic oxidative desulfurization performance. *Journal of Alloys and Compounds*. 661, 363-371. DOI: 10.1016/j.jallcom.2015.11.148.

[90] Li, M., Gao, X., Liu, H., Wang, H., Zhao, Q., Wang, N. (2020). Preparation of heterogeneous Fenton catalyst γ-Cu-Ce-Al_2O_3 and the evaluation on degradation of phenol. *Environmental Science and Pollution Research*. 27, 21476-21486. DOI: 10.1007/s11356-020-08648-w.

[91] Nguyen, A.T., Juang, R-S. (2015). Photocatalytic degradation of p-chlorophenol by hybrid H_2O_2 and TiO_2 in aqueous suspensions under UV irradiation. *Journal of Environmental Management*. 147, 271-277. DOI: 10.1016/j.jenvman.2014.08.023.

[92] Behnajady, M., Modirshahla, N., Shokri, M. (2004). Photodestruction of Acid Orange 7 (AO7) in aqueous solutions by UV/H_2O_2: influence of operational parameters. *Chemosphere*. 55, 129-134. DOI: 10.1016/j.chemosphere.2003.10.054.

[93] Galindo, C., Jacques, P., Kalt, A. (2001). Photochemical and photocatalytic degradation of an indigoid dye: a case study of acid blue 74 (AB74). *Journal of Photochemistry Photobiology A: Chemistry*. 141, 47-56. DOI: 10.1016/S1010-6030(01)00435-X.

[94] Rubio-Clemente, A., Chica, E., Penuela, G.A. (2017) Kinetic model describing the UV/H2O2 degradation of phenol in aqueous solutions. *Chemical Industry Chemical Engineering Quarterly*. 23, 547-562. DOI: 10.2298/CICEQ161119008R.

[95] Fetterolf, M.L., Patel, H.V., Jennings, J.M. (2003). Adsorption of Methylene Blue and Acid Blue 40 on Titania from Aqueous Solution. *Journal of Chemical Engineering Data*. 48, 831-835. DOI: 10.1021/je025589r.

[96] Mills, A., Le Hunte, S. (1997). An overview of semiconductor photocatalysis. *Journal of Photochemistry Photobiology A: Chemistry*. 108, 1-35. DOI: 10.1016/S1010-6030(97)00118-4.

[97] Rappoport, Z. (2003). The Chemistry of Phenols, Parts 1 and 2. Edited by (John Wiley & Sons).

[98] Sin, J.-C., Lam, S.-M., Lee, K.-T., Mohamed, A.R. (2013). Preparation and photocatalytic properties of visible light-driven samarium-doped ZnO nanorods. *Ceramics International*. 39, 5833-5843. DOI: 10.1016/j.ceramint.2013.01.004.

[99] Li Puma, G., Yue, P.L. (2002). Effect of the Radiation Wavelength on the Rate of Photocatalytic Oxidation of Organic Pollutants. *Industrial Engineering Chemistry Research*. 41, 5594-5600. DOI: 10.1021/ie0203274.

[100] Konstantinou, I.K., Albanis, T.A. (2004). TiO_2-assisted photocatalytic degradation of azo dyes in aqueous solution: kinetic and mechanistic investigations: A review. *Applied Catalysis B: Environmental*. 49, 1-14. DOI: 10.1016/j.apcatb.2003.11.010.

[101] Modirshahla, N., Hassani, A., Behnajady, M.A., Rahbarfam, R. (2011). Effect of operational parameters on decolorization of Acid Yellow 23 from wastewater by UV irradiation using ZnO and ZnO/SnO_2 photocatalysts. *Desalination*. 271, 187-192. DOI: 10.1016/j.desal.2010.12.027.

[102] Daneshvar, N., Rabbani, M., Modirshahla, N., Behnajady, M. (2004). Kinetic modeling of photocatalytic degradation of Acid Red 27 in UV/TiO_2 process. *Journal of Photochemistry Photobiology A: Chemistry*. 168, 39-45. DOI: 10.1016/j.jphotochem.2004.05.011.

[103] Chong, M.N., Jin, B., Chow, C.W., Saint, C. (2010). Recent developments in photocatalytic water treatment technology: A review. *Water Research*. 44, 2997-3027. DOI: 10.1016/j.watres.2010.02.039.

[104] Gaya, U.I., Abdullah, A.H. (2008). Heterogeneous photocatalytic degradation of organic contaminants over titanium dioxide: A review of fundamentals, progress and problems. *Journal of Photochemistry and Photobiology C: Photochemistry Reviews*. 9, 1-12. DOI: 10.1016/j.jphotochemrev.2007.12.003.

[105] Laoufi, N., Tassalit, D., Bentahar, F. (2008). The degradation of phenol in water solution by TiO_2 photocatalysis in a helical reactor. *Global NEST Journal*. 10, 404-418. DOI: 10.30955/gnj.000525

[106] Soltani, T., Entezari, M.H. (2014). Solar-Fenton catalytic degradation of phenolic compounds by impure bismuth ferrite nanoparticles synthesized via ultrasound. *Chemical Engineering Journal*. 251, 207-216. DOI: 10.1016/j.cej.2014.04.021.

[107] Gatou, M.-A., Fiorentis, E., Lagopati, N., Pavlatou, E.A. (2023). Photodegradation of Rhodamine B and Phenol Using TiO_2/SiO_2 Composite Nanoparticles: A Comparative Study. *Water*. 15, 2773. DOI: 10.3390/w15152773

[108] Molla, M., Tateishi, I., Furukawa, M., Katsumata, H., Suzuki, T., Knaeco, S., (2017). Evaluation of Reaction Mechanism for Photocatalytic Degradation of Dye with Self-Sensitized TiO_2 under Visible Light Irradiation. *Open Journal of Inorganic Non-metallic Materials*. 07, 1-7. DOI: 10.4236/ojinm.2017.71001.

[109] Paul, T., Das, D., Das, B.K., Sarkar, S., Maiti, S., Chattopadhyay, K.K. (2019). $CsPbBrCl_2$/g-C_3N_4 type II heterojunction as efficient visible range photocatalyst. *Journal of Hazardous Materials*. 380, 120855. DOI: 10.1016/j.jhazmat.2019.120855.

[110] Ghamarpoor, R., Fallah, A., Jamshidi, M. (2024). A Review of Synthesis Methods, Modifications, and Mechanisms of ZnO/TiO_2-Based Photocatalysts for Photodegradation of Contaminants. *ACS Omega*. 9, 25457-25492. DOI: 10.1021/acsomega.3c08717.